Available online at www.sciencedirect.com

SCIENCE DIRECT®

Comput. Methods Appl. Mech. Engrg. 195 (2006) 2533–2573

Computer methods in applied mechanics and engineering

www.elsevier.com/locate/cma

Integration of *hp*-adaptivity and a two grid solver for electromagnetic problems

D. Pardo [a,*], L. Demkowicz [a], J. Gopalakrishnan [b]

[a] *Institute for Computational Engineering and Sciences (ICES), The University of Texas at Austin, Austin, TX 78712, United States*
[b] *Department of Mathematics, University of Florida, Gainesville, FL 32611, United States*

Received 2 December 2004; received in revised form 25 May 2005; accepted 27 May 2005

Abstract

We present implementation details and analyze convergence of a two grid solver forming the core of a fully automatic *hp*-adaptive strategy for electromagnetic problems. The solver delivers a solution for a *fine* grid obtained from an arbitrary *coarse hp* grid by a global *hp*-refinement. The classical V-cycle algorithm combines an overlapping block Jacobi smoother with optimal relaxation, and a direct solve on the coarse grid. A theoretical analysis of the two grid solver is illustrated with numerical experiments. Several electromagnetic applications show the efficiency of combining the fully automatic *hp*-adaptive strategy with the two grid solver.

Keywords: Multigrid; Iterative solvers; Preconditioners; Maxwell's equations

---

1. Introduction

The paper is concerned with a construction and study of an iterative solver for linear systems resulting from *hp*-adaptive finite element (FE) discretizations of Maxwell's equations. Here, *h* stands for element size, and *p* denotes element order of approximation, both varying *locally* throughout the mesh.

The algorithm presented in [13,9] produces a sequence of optimally *hp*-refined meshes that delivers exponential convergence rates in terms of the FE error measured in energy norm vs the discrete problem size (number of degrees-of-freedom (d.o.f.)) or the CPU time. A given (coarse) *hp* mesh is first refined globally in *both h* and *p* to yield a *fine mesh*, i.e. each element is broken into four element-sons (eight in 3D), and the

---

[*] Corresponding author. Tel.: +1 512 471 3312; fax: +1 512 471 8694.
E-mail address: dzubiaur@yahoo.es (D. Pardo).

doi:10.1016/j.cma.2005.05.017

discretization order p is raised uniformly by one. We solve then the problem of interest on the fine mesh. The next *optimal coarse mesh* is determined by minimizing the *projection based interpolation error* of the fine mesh solution with respect to the optimally refined coarse mesh. The algorithm is very general, and it applies to H^1-, $H(\mathbf{curl})$-, and $H(\mathrm{div})$-conforming discretizations [12,10]. In particular, it is suitable for electromagnetic problems. Moreover, since the mesh optimization process is based on minimizing the interpolation error rather than the residual, the algorithm is problem independent, and it can be applied to non-linear and eigenvalue problems as well.

Critical to the success of the proposed adaptive strategy is the solution of the fine grid problem. Typically, in 3D, the global *hp*-refinement increases the problem size at least by one order of magnitude, making the use of an iterative solver inevitable. With a multigrid solver in mind, we choose to implement first a two grid solver based on the interaction between the coarse and fine *hp* meshes. The choice is quite natural. The coarse meshes are minimum in size. Also, for wave propagation problems in the frequency domain, the size of the coarsest mesh in the multigrid algorithm is limited by the condition that the mesh has to resolve all eigenvalues below the frequency of interest. Consequently, the sequence of multigrid meshes may be limited to just a few meshes only.

The fine mesh is obtained from the coarse mesh by the global *hp*-refinement. This guarantees that the corresponding FE spaces are nested, and allows for the standard construction of the prolongation and restriction operators. Notice that the sequence of optimal coarse *hp* meshes produced by the self-adaptive algorithm discussed above is *not* nested. The coarse meshes are highly non-uniform, both in element size h and order of approximation p, and they frequently include *anisotropically* refined elements (construction of multigrid algorithms for such anisotropically refined meshes is sometimes difficult), but the global refinement facilitates greatly the logic of implementation.

Customarily, any work on iterative methods starts with self-adjoint and positive definite problems, and this was the subject of the work presented in [25]. We included 2D and 3D examples of problems with highly non-homogeneous and anisotropic material data, as well as problems presenting corners and edge singularities.

In this paper, we are concerned with a construction of a similar but yet different two grid solver algorithm suitable for general electromagnetic (EM) problems. We also discuss advantages and limitations of the *hp*-adaptive strategy combined with the two grid solver when applied to real life EM problems.

The structure of our presentation is as follows. We begin with a formulation of the two grid solver algorithm, and a study of its convergence. In Section 3, we present some implementation details, while Section 4 is devoted to numerical experimentation. A number of EM applications is presented in Section 5. Conclusions are drawn in Section 6.

Notice that the two grid solver is not intended to be used only as a solver itself, but also as a crucial part of the *hp*-adaptive strategy. Among several implementation and theoretical issues that we address in this paper, one is especially important for us; is it possible to guide the optimal hp-refinements for EM problems with a partially converged fine grid solution only, and to what extent?

2. Formulation of the two grid solver

2.1. A stabilized variational formulation for solving the Maxwell's equations

At this point, we describe a mathematical formulation to solve the electromagnetic problem. Following [8], we consider a *bounded* domain $\Omega \subset \mathbb{R}^3$, with boundary Γ consisting of two disjoint parts Γ_1 and Γ_2. We wish to find electric field $\boldsymbol{E}(\boldsymbol{x}), \boldsymbol{x} \in \bar{\Omega}$, that satisfies:

- the reduced wave equation in Ω,

$$\nabla \times \left(\frac{1}{\mu}\nabla \times \boldsymbol{E}\right) - (\omega^2\epsilon - \mathrm{j}\omega\sigma)\boldsymbol{E} = -\mathrm{j}\omega\boldsymbol{J}^{\mathrm{imp}}, \tag{2.1}$$

- Dirichlet (ideal conductor) boundary condition on Γ_1,

$$\boldsymbol{n} \times \boldsymbol{E} = \boldsymbol{0}, \tag{2.2}$$

- Neumann boundary condition on Γ_2,

$$\boldsymbol{n} \times \left(\frac{1}{\mu}\nabla \times \boldsymbol{E}\right) = -\mathrm{j}\omega\boldsymbol{J}_{\mathrm{S}}^{\mathrm{imp}}. \tag{2.3}$$

Here, ω is an angular frequency, ϵ, μ, σ denote dielectric permittivity, magnetic permeability, and conductivity of the medium, $\boldsymbol{J}^{\mathrm{imp}}$ is a prescribed, impressed (source) current, $\boldsymbol{J}_{\mathrm{S}}^{\mathrm{imp}}$ is a prescribed, impressed surface current tangent to boundary Γ_2, $\boldsymbol{n} \cdot \boldsymbol{J}_{\mathrm{S}}^{\mathrm{imp}} = 0$, with n denoting the normal outward unit vector to Γ. Finally, j is the imaginary unit.

For theoretical reasons related to the proof of convergence for the two grid algorithm, presented in Section 2.4, we assume additionally that domain Ω is convex. This limitation seems to be of a theoretical nature, as no loss in performance for non-convex domains have been observed in presented numerical experiments.

For the sake of simplicity, we shall restrict ourselves to simply connected domains Ω only, avoiding the technical issues associated to *cohomology spaces*, see e.g. [7].

2.1.1. Standard variational formulation

The standard variational formulation is obtained by multiplying (2.1) by a vector test function $\bar{\boldsymbol{F}}$, integrating over domain Ω, integrating by parts, and using the Neumann boundary condition:

$$\left\{\begin{array}{l}\text{Find } \boldsymbol{E} \in H_D(\mathbf{curl};\Omega) \text{ such that}\\ \displaystyle\int_\Omega \frac{1}{\mu}(\nabla \times \boldsymbol{E})\cdot(\nabla \times \bar{\boldsymbol{F}})\,\mathrm{d}x - \int_\Omega (\omega^2\epsilon - \mathrm{j}\omega\sigma)\boldsymbol{E}\cdot\bar{\boldsymbol{F}}\,\mathrm{d}x\\ \displaystyle\quad = -\mathrm{j}\omega\int_\Omega \boldsymbol{J}^{\mathrm{imp}}\cdot\bar{\boldsymbol{F}}\,\mathrm{d}x + \mathrm{j}\omega\int_{\Gamma_2}\boldsymbol{J}_{\mathrm{S}}^{\mathrm{imp}}\cdot\bar{\boldsymbol{F}}\,\mathrm{d}S \quad \text{for all } \boldsymbol{F} \in H_D(\mathbf{curl};\Omega).\end{array}\right. \tag{2.4}$$

In the above $H_D(\mathbf{curl};\Omega)$ is the Hilbert *space of admissible solutions*

$$\boldsymbol{H}_D(\mathbf{curl};\Omega) := \{\boldsymbol{E} \in \boldsymbol{L}^2(\Omega) : \nabla \times \boldsymbol{E} \in \boldsymbol{L}^2(\Omega),\ \boldsymbol{n} \times \boldsymbol{E} = \boldsymbol{0} \text{ on } \Gamma_1\}, \tag{2.5}$$

with inner product defined by

$$(\boldsymbol{u},\boldsymbol{v})_{H_D(\mathbf{curl};\Omega)} := (\boldsymbol{u},\boldsymbol{v})_{\boldsymbol{L}^2(\Omega)} + (\nabla \times \boldsymbol{u}, \nabla \times \boldsymbol{v})_{\boldsymbol{L}^2(\Omega)}. \tag{2.6}$$

The original and variational formulations are equivalent to each other.

2.1.2. Stabilized variational formulation

Introducing a *space of Lagrange multipliers* (scalar potentials):

$$H^1_D(\Omega) := \{q \in H^1(\Omega) : q = 0 \text{ on } \Gamma_1\}, \tag{2.7}$$

we employ a special test function $\boldsymbol{F} = \nabla q, q \in H^1_D(\Omega)$, to discover that solution $\boldsymbol{E}$ to the variational formulation must *automatically* satisfy the weak form of the continuity equation

$$-\int_\Omega (\omega^2\epsilon - \mathrm{j}\omega\sigma)\boldsymbol{E}\cdot\boldsymbol{\nabla}\bar{q}\,\mathrm{d}x = -\mathrm{j}\omega\int_\Omega \boldsymbol{J}^{\mathrm{imp}}\cdot\boldsymbol{\nabla}\bar{q}\,\mathrm{d}x + \mathrm{j}\omega\int_{\Gamma_2}\boldsymbol{J}_{\mathrm{S}}^{\mathrm{imp}}\cdot\boldsymbol{\nabla}\bar{q}\,\mathrm{d}S. \tag{2.8}$$

We also recall the Helmholtz decomposition:

$$\boldsymbol{E} = \boldsymbol{\nabla}\phi + \boldsymbol{E}_0, \quad \text{where } \phi \in H^1_D(\Omega) \text{ and } (\boldsymbol{E}_0, \boldsymbol{\nabla}q)_{\boldsymbol{L}^2(\Omega)} = 0\ \forall q \in H^1_D(\Omega). \tag{2.9}$$

It is well-known that the standard variational formulation is *not* uniformly stable with respect to the wave number $k^2 = \mu(\omega^2\epsilon - \mathrm{j}\omega\sigma)$. As $k \to 0$, we loose the control over gradients. This corresponds to the fact that, in the limiting case $k = 0$, the problem is ill-posed as the gradient component remains undetermined. A remedy to this problem is to enforce the continuity equation explicitly at the expense of introducing a Lagrange multiplier $p \in H^1_D(\Omega)$. The so-called *stabilized variational formulation* looks as follows:

$$\begin{cases} \text{Find } \boldsymbol{E} \in H_D(\mathbf{curl};\Omega),\ p \in H^1_D(\Omega) \text{ such that} \\ \displaystyle\int_\Omega \frac{1}{\mu}(\boldsymbol{\nabla}\times\boldsymbol{E})(\boldsymbol{\nabla}\times\bar{\boldsymbol{F}})\,\mathrm{d}x - \int_\Omega(\omega^2\epsilon - \mathrm{j}\omega\sigma)\boldsymbol{E}\cdot\bar{\boldsymbol{F}}\,\mathrm{d}x \\ \displaystyle -\int_\Omega(\omega^2\epsilon - \mathrm{j}\omega\sigma)\boldsymbol{\nabla}p\cdot\bar{\boldsymbol{F}}\,\mathrm{d}x = -\mathrm{j}\omega\int_\Omega \boldsymbol{J}^{\mathrm{imp}}\cdot\bar{\boldsymbol{F}}\,\mathrm{d}x + \mathrm{j}\omega\int_{\Gamma_2}\boldsymbol{J}_{\mathrm{S}}^{\mathrm{imp}}\cdot\bar{\boldsymbol{F}}\,\mathrm{d}S \\ \quad \forall \boldsymbol{F} \in H_D(\mathbf{curl};\Omega), \\ \displaystyle\int_\Omega(\omega\epsilon - j\sigma)\boldsymbol{E}\cdot\boldsymbol{\nabla}\bar{q}\,\mathrm{d}x = -j\int_\Omega \boldsymbol{J}^{\mathrm{imp}}\cdot\boldsymbol{\nabla}\bar{q}\,\mathrm{d}x + j\int_{\Gamma_2}\boldsymbol{J}_{\mathrm{S}}^{\mathrm{imp}}\cdot\boldsymbol{\nabla}\bar{q}\,\mathrm{d}S \\ \quad \forall q \in H^1_D(\Omega). \end{cases} \tag{2.10}$$

By repeating the trick with the substitution $\boldsymbol{F} = \boldsymbol{\nabla}q$ in the first equation, we discover that the Lagrange multiplier *p identically vanishes*, and for that reason, it is frequently called the *hidden variable*. In comparison with the original formulation, the stability constant for the regularized formulation converges to zero slower as $k \to 0$. In the case when $\sigma = 0$, and the right-hand side of the second equation vanishes, we can divide the second equation by another ω to obtain

$$-\int_\Omega \epsilon\boldsymbol{E}\cdot\boldsymbol{\nabla}\bar{q}\,\mathrm{d}x = 0. \tag{2.11}$$

In this case, the inf–sup stability constant converges to one as $\omega \to 0$. The regularized formulation works because gradients of the scalar-valued potentials from $H^1_D(\Omega)$ form precisely the null space of the curl–curl operator.

The point about the stabilized (mixed) formulation is that, whether we use it or not in the actual computations (the improved stability is one good reason to do it), the original variational problem is *equivalent* to the mixed problem.

2.2. Formulation of the two grid solver for EM

Solving a linear system of equations (using a multigrid scheme) arising from Maxwell's equations is challenging mainly for two reasons: the linear system is (in general) indefinite, and the null space of the differential operator **curl** is large.

The problem of indefiniteness of the linear system can be overcome by requesting the coarse grid to be fine enough (see, for example, [6,16]). This assumption is needed both to define a block Jacobi smoother, as well as to prove convergence of the overall two grid solver algorithm.

In order to control the solution over the null space of the **curl**, we may utilize Helmholtz decomposition (2.12), and treat both terms separately:

$$H_D(\mathbf{curl};\Omega) = (\mathrm{Ker}(\mathbf{curl})) \oplus (\mathrm{Ker}(\mathbf{curl}))^\perp. \tag{2.12}$$

Two corresponding decompositions have been constructed for lower order FE spaces. More precisely, let T be a grid, M the associated lowest order Nedelec subspaces of $H_D(\mathbf{curl};\Omega)$ of the first kind [24], and W the corresponding first order piecewise polynomial subspace of $H^1_D(\Omega)$. Let, v_l (resp. e_l) denote the non-Dirichlet vertexes (resp. edges) of the grid T. Then, we define

$$\Omega_l^v = \mathrm{int}\Big(\bigcup\{\bar{L} \in T : v_l \in \partial L\}\Big), \tag{2.13}$$

$$\Omega_l^e = \mathrm{int}\Big(\bigcup\{\bar{L} \in T : e_l \in \partial L\}\Big). \tag{2.14}$$

And

$$M_l^v = \{u \in M : \mathrm{supp}(u) \subset \Omega_l^v\};\ M_l^e = \{u \in M : \mathrm{supp}(u) \subset \Omega_l^e\}, \tag{2.15}$$

$$W_l^v = \{u \in W : \mathrm{supp}(u) \subset \Omega_l^v\};\ W_l^e = \{u \in W : \mathrm{supp}(u) \subset \Omega_l^e\} = \emptyset\ . \tag{2.16}$$

We have the decomposition:

$$W = \sum_v W_l^v. \tag{2.17}$$

Arnold et al. [2] proposed the following decomposition of M:

$$M = \sum_v M_l^v, \tag{2.18}$$

which we shall call the AFW decomposition. Another well-known decomposition of M is Hiptmair's decomposition [19]:

$$M = \sum_e M_l^e + \sum_v \nabla W_l^v. \tag{2.19}$$

Each decomposition, together with the already prescribed coarse grid, determines a two grid solver in terms of a multigrid framework, as presented, for example, in [5]. More precisely, the bilinear form defined over each subspace can be inverted, generating a block Jacobi (or Gauss–Seidel) smoother for the fine grid that, together with the coarse grid, define a two grid solver algorithm.

A formal generalization of these decompositions for *hp*-edge elements is straightforward. Notice that Hiptmair's decomposition (with lowest order elements) utilizes only one-dimensional subspaces (and therefore, point smoothers), while the AFW decomposition utilizes four-dimensional subspaces. For higher order elements, size of patches will become considerably larger as p increases and, as a consequence, amount of memory (and number of operations) required by the corresponding block Jacobi smoothers become prohibitive. Thus, a suitable two grid solver algorithm for *hp*-edge FE may come from combining the ideas presented in [25] with Hiptmair's approach to control gradients.

In the remainder of this section, we present a two grid solver algorithm that combines a generalization of Hiptmair's approach to *hp*-edge FE with the block Jacobi smoother presented in [25]. M and W will denote the *hp*-FE subspaces of $H_D(\mathbf{curl})$ and H^1_D, respectively.

We will illustrate via numerical experiments the importance of an adequate control of the kernel of the **curl** operator formed by gradients of potentials. Indeed, a two grid solver may not converge if the gradients are not resolved correctly.

2.2.1. Overlapping block Jacobi smoothers

At this point, we define two overlapping block Jacobi smoothers:

- one used as a preconditioner for the electric field, given by

$$\mathbf{S_E} = \sum_{l=1}^{N} \boldsymbol{\iota}_l \boldsymbol{D}_l^{-1} \boldsymbol{\iota}_l^{\mathrm{T}},$$

- and another used as a preconditioner for the gradients, given by

  $$\mathbf{S}_{\nabla} = \sum_{l=1}^{N} \boldsymbol{\imath}_{\nabla,l} \boldsymbol{D}_{\nabla,l}^{-1} \boldsymbol{\imath}_{\nabla,l}^{\mathrm{T}}.$$

  Here, $\boldsymbol{D}_l$ denotes the diagonal sub-block of global stiffness matrix $\boldsymbol{A}$ corresponding to d.o.f. of a particular (modified) element that span an *hp*-edge FE subspace $M_l \subset H_D(\mathbf{curl};\Omega)$. $\boldsymbol{D}_{\nabla,l}$ denotes the diagonal sub-block of global mass matrix for the gradients (Laplace equation) $\boldsymbol{A}_{\nabla}$ corresponding to d.o.f. of a particular (modified) element that span an *hp* FE subspace $W_l \subset H_D^1(\Omega)$. $\boldsymbol{\imath}_l$, $\boldsymbol{\imath}_{\nabla,l}$ are the matrices associated with the natural embeddings from M_l into M, and ∇W_l into M, respectively.

At this point, we would like to simplify our notation and drop the boldface symbols for the matrices and vectors in the coefficient space.

2.2.2. An approximation to the optimal relaxation parameter

An optimal relaxation parameter was selected in [25] to minimize the error in the energy norm, which turned out to be a computable number for self-adjoint positive definite (SPD) problems. For electrodynamic problems, computation of the optimal relaxation parameter involves solution of the system of linear equations that we are trying to solve. Thus, only an approximation to it may be available.

Since $S \approx A^{-1}$, we define our approximation to the optimal relaxation parameter as the argument that minimizes Sr in the energy norm. Thus, at step n, $\alpha^{(n)}$ is given by

$$\alpha^{(n)} = \arg\min_{\alpha} \|Sr^{(n+1)}(\alpha)\|_B = \arg\min_{\alpha} \|S(I - \alpha A r^{(n)})\|_B = \frac{(Sr^{(n)}, SASr^{(n)})_B}{(SASr^{(n)}, SASr^{(n)})_B}, \tag{2.20}$$

where B is the mass matrix associated with the energy norm ($(Bu,v) = (u,v)_{H_D(\mathbf{curl})}$), and S is either S_E or S_{∇}.

2.3. The two grid algorithm

We define our two grid solver (based on a modification of Hiptmair's decomposition) as the iteration along the following steps. Given current solution x, and residual r, we perform,

(1) *Coarse grid correction*, i.e.,
  - restrict the residual to the coarse grid dual space,

    $$r_0 = Q^{\mathrm{T}} r, \tag{2.21}$$

  - solve the coarse grid problem for coarse grid correction Δx_0,

    $$A_0 \Delta x_0 = r_0, \tag{2.22}$$

  - prolong the coarse grid correction to the fine grid space, and compute the corresponding correction for the residual,

    $$\Delta x = Q \Delta x_0, \quad \Delta r = A \Delta x, \tag{2.23}$$

  - update the fine grid solution and residual,

    $$\begin{aligned} x &= x + \Delta x, \\ r &= r - \Delta r. \end{aligned} \tag{2.24}$$

(2) *Block Jacobi smoother on the fine grid*, i.e.,
  - compute the smoothing correction and the corresponding correction for the residual,

    $$\Delta x = S_E r, \quad \Delta r = A \Delta x, \tag{2.25}$$

- compute an approximation of the optimal relaxation parameter α,

$$\alpha_E = \frac{(S_E r, S_E A S_E r)_B}{(S_E A S_E r, S_E A S_E r)_B}, \tag{2.26}$$

- update the solution and residual,

$$\begin{aligned} x &= x + \alpha_E \Delta x, \\ r &= r - \alpha_E \Delta r. \end{aligned} \tag{2.27}$$

(3) *Block Jacobi smoother to control gradients*, i.e.,

- compute the smoothing correction and the corresponding correction for the gradients of the residual,

$$\Delta x = S_\nabla r, \quad \Delta r = A \Delta x, \tag{2.28}$$

- compute an approximation of the optimal relaxation parameter α,

$$\alpha_\nabla = \frac{(S_\nabla r, S_\nabla A S_\nabla r)_B}{(S_\nabla A S_\nabla r, S_\nabla A S_\nabla r)_B}, \tag{2.29}$$

- update the solution and residual,

$$\begin{aligned} x &= x + \alpha_\nabla \Delta x, \\ r &= r - \alpha_\nabla \Delta r. \end{aligned} \tag{2.30}$$

2.4. Convergence theory

A proof of convergence for our two grid solver algorithm can be inferred from the convergence theory for multigrid algorithms presented in [16], which refers to [15,19], and [2] among others, for detailed proofs. In here, we outline the main ingredients of the convergence proof, which can be divided into three parts:

- First, we introduce some notation and a discrete Poincaré–Friedrichs type inequality, necessary to define our block Jacobi smoothers.
- Next, we define an auxiliary problem, which differs from our original problem in the value of wave number (squared) k^2. By setting $k^2 = -1$, we obtain a SPD auxiliary problem with convergence properties in terms of the two grid solver equivalent (up to a constant times element size h) to our original problem, under the assumption that the coarse grid is fine enough.
- Finally, we prove convergence of our two grid algorithm for the auxiliary SPD problem with a contraction constant independent of h, and possibly depending upon polynomial order of approximation p. Thus, convergence of the two grid solver for the original problem is guaranteed.

We assume that k^2 is real and such that our boundary value problem given by Eqs. (2.1)–(2.3) has a unique solution. In the following, we will attempt to trace the dependence of various constants such as: wave number k, mesh size h, and polynomial order of approximation p. C will denote a generic positive constant independent of h, p, and k. A subindex h, p, or k will denote dependence upon h, p, or k, respectively. For example, C_p will denote a generic positive constant independent of h and k, but possibly dependent upon p.

We assume that our subspace decomposition $M = \sum M_l$ is such that the discrete Friedrichs inequality holds, i.e.:

$$\|\mathbf{q}_l\|_{L^2} \leqslant Ch \|\nabla \times \mathbf{q}_l\|_{L^2} \quad \forall \mathbf{q}_l \in \check{M}_l, \quad l \geqslant 1, \tag{2.31}$$

where $\check{M}_l = \{\mathbf{q}_l \in M_l : (\mathbf{q}_l, \nabla\phi_l)_{L^2} = 0\ \forall\phi_l \in W_l\}$, and $\nabla W_l = \{q_l \in M_l : \nabla \times q_l = 0\} \subset M_l$. This inequality has been proved for a variety of space decompositions, including spaces corresponding to local Dirichlet problems for *hp*-meshes (see, for example, [10,11,14]).

Using the discrete Friedrichs inequality we can prove the following result.

Proposition 1. *Let* $\mathbf{q}_l \in M_l$ $(l \geqslant 1)$ *be a solution of problem,*

$$A(\mathbf{q}_l, \mathbf{v}_l) = A(\mathbf{u}, \mathbf{v}_l) \quad \forall \mathbf{v}_l \in M_l, \tag{2.32}$$

where $\mathbf{u} \in M$, *and* $A(,)$ *is the bilinear form associated to our variational formulation. Then*

$$\|\mathbf{q}_l\|_{H_D(\mathbf{curl},\Omega_l)} \leqslant C_{hk}\|\mathbf{u}\|_{H_D(\mathbf{curl},\Omega_l)}, \tag{2.33}$$

where supp $\mathbf{q}_l \subset \{\Omega_l, \forall \mathbf{q}_l \in M_l\}$, *and* $C_{hk} = \frac{\max\{1,k^2\}}{\min\{1-C^2h^2(k^2+1),k^2\}}$. *It follows that, if* $h^2(k^2+1)$ *is small enough, then the local problems have unique solutions, and therefore, the corresponding block Jacobi smoothers are well-defined.*

Proof. Using discrete Helmholtz decomposition, we have

$$\mathbf{q}_l = \mathbf{q}_{l,1} + \mathbf{q}_{l,2}, \quad (\mathbf{q}_{l,1}, \mathbf{q}_{l,2})_{L^2} = 0, \tag{2.34}$$

where $\mathbf{q}_{l,1} \in \check{M}_l$, and $\mathbf{q}_{l,2} = \nabla\phi$ for some $\phi \in W_l$.

Substituting $\mathbf{v}_l = \mathbf{q}_l$ in (2.32), and recalling the definition of bilinear form $A(,)$, we obtain

$$\begin{aligned}&(\nabla \times \mathbf{q}_{l,1}, \nabla \times \mathbf{q}_{l,1})_{L^2} - k^2(\mathbf{q}_{l,1}, \mathbf{q}_{l,1})_{L^2} - k^2(\mathbf{q}_{l,2}, \mathbf{q}_{l,2})_{L^2}\\ &\quad = (\nabla \times \mathbf{u}, \nabla \times \mathbf{q}_{l,1})_{L^2} - k^2(\mathbf{u}, \mathbf{q}_{l,1})_{L^2} - k^2(\mathbf{u}, \mathbf{q}_{l,2})_{L^2}.\end{aligned} \tag{2.35}$$

Setting $\mathbf{v}_l = \mathbf{q}_{l,2}$ in (2.32), we have

$$k^2(\mathbf{q}_{l,2}, \mathbf{q}_{l,2})_{L^2} = k^2(\mathbf{u}, \mathbf{q}_{l,2})_{L^2}. \tag{2.36}$$

Thus

$$(\mathbf{q}_{l,1}, \mathbf{q}_{l,1})_{H_D(\mathbf{curl})} - (k^2+1)(\mathbf{q}_{l,1}, \mathbf{q}_{l,1})_{L^2} = (\nabla \times \mathbf{u}, \nabla \times \mathbf{q}_{l,1})_{L^2} - k^2(\mathbf{u}, \mathbf{q}_{l,1})_{L^2}. \tag{2.37}$$

Since $\mathbf{q}_{l,1}$ is discrete divergence free (i.e., $\mathbf{q}_{l,1} \in \check{M}_l$), we can apply Friedrichs inequality on the left-hand side:

$$\|\mathbf{q}_{l,1}\|^2_{H_D(\mathbf{curl})} - (k^2+1)\|\mathbf{q}_{l,1}\|^2_{L^2} \geqslant [1 - C^2h^2(k^2+1)]\|\mathbf{q}_{l,1}\|^2_{H_D(\mathbf{curl})}. \tag{2.38}$$

Dividing last equation by $\|\mathbf{q}_{l,1}\|_{H_D(\mathbf{curl})}$, and applying Eq. (2.37), we obtain

$$[1 - C^2h^2(k^2+1)]\|\mathbf{q}_{l,1}\|_{H_D(\mathbf{curl})} \leqslant \sup_{\mathbf{q}_{l,1} \in \check{M}_l} \frac{(\nabla \times \mathbf{u}, \nabla \times \mathbf{q}_{l,1})_{L^2} - k^2(\mathbf{u}, \mathbf{q}_{l,1})_{L^2}}{\|\mathbf{q}_{l,1}\|_{H_D(\mathbf{curl})}}. \tag{2.39}$$

From Eq. (2.36), we derive for $\mathbf{q}_{l,2}$ that

$$k^2\|\mathbf{q}_{l,2}\|_{H_D(\mathbf{curl})} \leqslant \sup_{\mathbf{q}_{l,2} = \nabla\psi, \psi \in W_l} \frac{(\nabla \times \mathbf{u}, \nabla \times \mathbf{q}_{l,2})_{L^2} - k^2(\mathbf{u}, \mathbf{q}_{l,2})_{L^2}}{\|\mathbf{q}_{l,2}\|_{H_D(\mathbf{curl})}}. \tag{2.40}$$

Using (2.39) and (2.40), and the orthogonality of Hilbert spaces $\check{M}_l$ and ∇W_l, we conclude

$$\begin{aligned}[1 - C^2h^2(k^2+1)]^2\|\mathbf{q}_{l,1}\|^2_{H_D(\mathbf{curl})} + k^4\|\mathbf{q}_{l,2}\|^2_{H_D(\mathbf{curl})} &\leqslant \left(\sup_{\mathbf{q}_l \in M_l} \frac{(\nabla \times \mathbf{u}, \nabla \times \mathbf{q}_l)_{L^2} - k^2(\mathbf{u}, \mathbf{q}_l)_{L^2}}{\|\mathbf{q}_l\|_{H_D(\mathbf{curl})}}\right)^2\\ &\leqslant (\|\nabla \times \mathbf{u}\|_{L^2} + k^2\|\mathbf{u}\|_{L^2})^2\end{aligned} \tag{2.41}$$

and the result follows, since

$$(\|\mathbf{q}_{l,1}\|^2_{H_D(\mathbf{curl})} + \|\mathbf{q}_{l,2}\|^2_{H_D(\mathbf{curl})})^{1/2} \leqslant \frac{\max\{1,k^2\}}{\min\{1 - C^2h^2(k^2+1), k^2\}}. \qquad \square \tag{2.42}$$

As a consequence of the proposition, the $A(\,,)$-projection $\mathbf{P}_l{:}H_D(\mathbf{curl}) \to M_l$ satisfies

$$\|\mathbf{P}_l\mathbf{u}\|_{H_D(\mathbf{curl})} \leqslant \frac{\max\{1,k^2\}}{\min\{1 - C^2h^2(k^2+1), k^2\}}\|\mathbf{u}\|_{H_D(\mathbf{curl})}. \tag{2.43}$$

At this point, we consider an auxiliary boundary value problem given again by Eqs. (2.1)–(2.3), but with $k^2 = -1$. And we denote operators associated to our SPD auxiliary problem with the $\sim$ symbol. For example, $\widetilde{\mathbf{P}}_l$.

In the following, we show that the convergence properties of the two grid solver for the original and auxiliary problems are comparable up to a perturbation term. Such results were first proved for the Helmholtz equation in [6]. That they can be extended to the Maxwell case, notwithstanding the non-ellipticity, was realized in [15]. The following perturbation lemma is proved along the lines of a similar result in [16]:

Lemma 1. *For all* $l \geqslant 1$, *we have*

$$\|\mathbf{P}_l - \widetilde{\mathbf{P}}_l\|_{H_D(\mathbf{curl})} \leqslant C(1 + C_{hk})(k^2+1)h, \tag{2.44}$$

where $C_{hk} = \frac{\max\{1,k^2\}}{\min\{1-C^2h^2(k^2+1),k^2\}}$.

Proof. Let $u, q \in H_D(\mathbf{curl})$. Since $\tilde{\mathbf{P}}_l$ is an $H_D(\mathbf{curl})$-projection, we obtain the following identity:

$$\begin{aligned}(\mathbf{P}_l\mathbf{u} - \widetilde{\mathbf{P}}_l\mathbf{u}, \mathbf{q})_{H_D(\mathbf{curl})} &= (\mathbf{P}_l\mathbf{u} - \mathbf{u}, \widetilde{\mathbf{P}}_l\mathbf{q})_{H_D(\mathbf{curl})} = A(\mathbf{P}_l\mathbf{u} - \mathbf{u}, \widetilde{\mathbf{P}}_l\mathbf{q}) + (k^2+1)(\mathbf{P}_l\mathbf{u} - \mathbf{u}, \widetilde{\mathbf{P}}_l\mathbf{q})_{L^2} \\ &= (k^2+1)(\mathbf{P}_l\mathbf{u} - \mathbf{u}, \widetilde{\mathbf{P}}_l\mathbf{q})_{L^2}.\end{aligned} \tag{2.45}$$

Now, using discrete Helmholtz decomposition (and notation of Proposition 1):

$$(\mathbf{u} - \mathbf{P}_l\mathbf{u}, \mathbf{q}_l)_{L^2} = (\mathbf{u} - \mathbf{P}_l\mathbf{u}, \mathbf{q}_{l,1})_{L^2} + (\mathbf{u} - \mathbf{P}_l\mathbf{u}, \mathbf{q}_{l,2})_{L^2}. \tag{2.46}$$

Since $\mathbf{q}_{l,2} = \nabla\phi_l$:

$$-k^2(\mathbf{u} - \mathbf{P}_l\mathbf{u}, \mathbf{q}_{l,2})_{L^2} = A(\mathbf{u} - \mathbf{P}_l\mathbf{u}, \mathbf{q}_{l,2}) = 0. \tag{2.47}$$

Applying Cauchy–Schwarz inequality, followed by discrete Friedrichs inequality, we obtain

$$(\mathbf{u} - \mathbf{P}_l\mathbf{u}, \mathbf{q}_{l,1})_{L^2} \leqslant Ch\|\mathbf{u} - \mathbf{P}_l\mathbf{u}\|_{L^2(\Omega_l)}\|\nabla \times \mathbf{q}_{l,1}\|_{L^2(\Omega_l)}. \tag{2.48}$$

Thus

$$(\mathbf{P}_l\mathbf{u} - \widetilde{\mathbf{P}}_l\mathbf{u}, \mathbf{q})_{H_D(\mathbf{curl})} \leqslant Ch(k^2+1)\|\mathbf{u} - \mathbf{P}_l\mathbf{u}\|_{L^2(\Omega_l)}\|\nabla \times \widetilde{\mathbf{P}}_l\mathbf{q}\|_{L^2(\Omega_l)}. \tag{2.49}$$

From (2.43) we obtain

$$\|\mathbf{u} - \mathbf{P}_l\mathbf{u}\|_{L^2(\Omega_l)} \leqslant (1 + C_{hk})\|\mathbf{u}\|_{H_D(\mathbf{curl},\Omega_l)}. \tag{2.50}$$

Finally,

$$\|\nabla \times \widetilde{\mathbf{P}}_l\mathbf{q}\|_{L^2(\Omega_l)} \leqslant \|\mathbf{q}\|_{H_D(\mathbf{curl},\Omega_l)} \tag{2.51}$$

And the result follows. $\square$

The following lemma quantifies the difference between the definite and the indefinite coarse solves that appears in the algorithm. The proof is similar to the proof of [15, Lemma 4.3] (also cf. [23]) but we now keep track of the dependence of the constants on polynomial degree using the recent results in [10,11].

Lemma 2. *If domain Ω is convex, we have*

$$\|\mathbf{P}_0 - \widetilde{\mathbf{P}}_0\|_{H_D(\mathbf{curl})} \leqslant C_k \frac{h}{p^{1/2-\epsilon}\sqrt{1 - C_k' \dfrac{h}{p^{1/2-\epsilon}}}}, \tag{2.52}$$

where $\epsilon > 0$.

Proof. Eqs. (2.45)–(2.47) are valid also for coarse grid subspace M_0. We have for all $\mathbf{u}, \mathbf{q} \in M$:

$$(\mathbf{P}_0\mathbf{u} - \widetilde{\mathbf{P}}_0\mathbf{u}, \mathbf{q})_{H_D(\mathbf{curl})} = (k^2+1)(\mathbf{u} - \mathbf{P}_0\mathbf{u}, -\mathbf{q}_{0,1})_{L^2}, \tag{2.53}$$

where $\mathbf{q}_{0,1}$ is the discrete divergence free part of $\mathbf{q}_0 = \widetilde{\mathbf{P}}_0\mathbf{q}$.

We define $\mathbf{e} = \mathbf{P}_0\mathbf{u} - \mathbf{u}$, with $\mathbf{e}_1$, $\mathbf{e}_2$ denoting the corresponding terms of the discrete Helmholtz decomposition of $\mathbf{e}$. Then

$$(\mathbf{P}_0\mathbf{u} - \widetilde{\mathbf{P}}_0\mathbf{u}, \mathbf{q})_{H_D(\mathbf{curl})} = (k^2+1)[(\mathbf{e}_1, \mathbf{q}_{0,1})_{L^2} + (\mathbf{e}_2, \mathbf{q}_{0,1})_{L^2}]. \tag{2.54}$$

In order to estimate both terms on the right hand side, we show first (following [15]) that

$$\|\mathbf{e}_1\|_{L^2} \leqslant C_k \frac{h}{p^{1/2-\epsilon}} \|\mathbf{e}\|_{H_D(\mathbf{curl})}. \tag{2.55}$$

We define $\mathbf{e}^1, \mathbf{q}^{0,1} \in H_D(\mathbf{curl})$ by the following conditions:

$$\begin{aligned} &\nabla \times \mathbf{e}^1 = \nabla \times \mathbf{e}_1; \quad (\mathbf{e}^1, \nabla\phi) = 0, \ \forall \phi \in H^1_D, \\ &\nabla \times \mathbf{q}^{0,1} = \nabla \times \mathbf{q}_{0,1}; \quad (\mathbf{q}^{0,1}, \nabla\phi) = 0 \ \forall \phi \in H^1_D. \end{aligned} \tag{2.56}$$

The following result has been proved in [3] for square elements using the technique of projection-based interpolation,[1]

$$\|\mathbf{e}_1 - \mathbf{e}^1\|_{L^2} \leqslant C \frac{h}{p^{1/2-\epsilon}} \|\nabla \times \mathbf{e}_1\|_{L^2}. \tag{2.57}$$

Here, $\epsilon > 0$ is an arbitrary small number, and $C = C(\epsilon) \to \infty$, as $\epsilon \to 0$.

With discrete divergence free $\mathbf{e}$, *replaced with pointwise divergence free* field $\mathbf{e}^1$, we turn now to the standard duality argument and consider solution $\mathbf{w}^1 \in H_D(\mathbf{curl})$ to the dual problem:

$$A(\mathbf{p}, \mathbf{w}^1) = (\mathbf{e}^1, \mathbf{p}) \quad \forall \mathbf{p} \in H_D(\mathbf{curl}). \tag{2.58}$$

With the assumption on convexity of the domain, we have

$$\|\mathbf{w}^1\|_{H^1(\mathbf{curl})} \leqslant C_k \|\mathbf{e}^1\|_{L^2}, \tag{2.59}$$

where $\|\mathbf{w}^1\|^2_{H^1(\mathbf{curl})} = \|\mathbf{w}^1\|^2_{H^1} + \|\nabla \times \mathbf{w}^1\|^2_{H^1}$.

Using the standard duality argument, and the fact that w^1 is divergence free, we obtain,

$$\begin{aligned} \|\mathbf{e}^1\|_{L^2} &\leqslant A(\mathbf{e}^1, \mathbf{w}^1) = A(\mathbf{e}_1, \mathbf{w}^1) = A(\mathbf{e}, \mathbf{w}^1) = A(\mathbf{e}, \mathbf{w}^1 - \Pi^{\text{curl}}\mathbf{w}^1) \\ &\leqslant C_k \|\mathbf{e}_1\|_{H_D(\mathbf{curl})} \cdot \|\mathbf{w}^1 - \Pi^{\text{curl}}\mathbf{w}^1\|_{H_D(\mathbf{curl})}, \end{aligned} \tag{2.60}$$

where Π^{curl} is the projection-based interpolation operator.

---

[1] An analogous result holds for triangular elements under a conjecture of an L^2-stability result, see [4].

From the approximation theory in [10,11], we obtain

$$\|\mathbf{w}^1 - \Pi^{\text{curl}}\mathbf{w}^1\|_{H_D(\mathbf{curl})} \leqslant C\frac{h}{p^{1-\epsilon}}\|\mathbf{w}^1\|_{H^1(\mathbf{curl})} \leqslant C_k\frac{h}{p^{1-\epsilon}}\|\mathbf{e}^1\|_{L^2}. \tag{2.61}$$

Application of triangle inequality finishes proof of (2.55).

Now, since $\mathbf{q}^{0,1}$ is divergence free, using Cauchy–Schwarz inequality, and estimate (2.57) for function $\mathbf{q}^{0,1}$, we obtain

$$\begin{aligned}(\mathbf{e}_2,\mathbf{q}_{0,1})_{L^2} &= (\mathbf{e}_2,\mathbf{q}_{0,1}-\mathbf{q}^{0,1})_{L^2} \leqslant \|\mathbf{e}_2\|_{L^2}\|\mathbf{q}_{0,1}-\mathbf{q}^{0,1}\|_{L^2} \leqslant C\frac{h}{p^{1/2-\epsilon}}\|\mathbf{e}\|_{L^2}\|\boldsymbol{\nabla}\times\mathbf{q}_{0,1}\|_{L^2} \\ &\leqslant C\frac{h}{p^{1/2-\epsilon}}\|\mathbf{e}\|_{H_D(\mathbf{curl})}\|\mathbf{q}\|_{H_D(\mathbf{curl})}.\end{aligned} \tag{2.62}$$

Similarly, using Cauchy–Schwarz inequality, and estimate (2.55), we get

$$(\mathbf{e}_1,\mathbf{q}_{0,1})_{L^2} \leqslant \|\mathbf{e}_1\|_{L^2}\|\mathbf{q}_{0,1}\|_{L^2} \leqslant C_k\frac{h}{p^{1/2-\epsilon}}\|\mathbf{e}\|_{H_D(\mathbf{curl})}\|\mathbf{q}\|_{H_D(\mathbf{curl})}. \tag{2.63}$$

Thus

$$(\mathbf{P}_0\mathbf{u}-\widetilde{\mathbf{P}}_0\mathbf{u},\mathbf{q})_{H_D(\mathbf{curl})} \leqslant C_k\frac{h}{p^{1/2-\epsilon}}\|\mathbf{e}\|_{H_D(\mathbf{curl})}\|\mathbf{q}\|_{H_D(\mathbf{curl})}. \tag{2.64}$$

In order to finish the proof for this lemma, it only remains to show that $\|\mathbf{e}\|_{H_D(\mathbf{curl})} \leqslant C_k\frac{1}{\sqrt{1-C_k' h/p^{1/2-\epsilon}}}\|\mathbf{u}\|_{H_D(\mathbf{curl})}$. This can be done as follows:

$$\begin{aligned}\|\mathbf{e}\|^2_{H_D(\mathbf{curl})} &= \|\mathbf{u}-\mathbf{P}_0\mathbf{u}\|^2_{H_D(\mathbf{curl})}, \\ &= A(\mathbf{u}-\mathbf{P}_0\mathbf{u},\mathbf{u}-\widetilde{\mathbf{P}}_0\mathbf{u}) + (1+k^2)(\mathbf{u}-\mathbf{P}_0\mathbf{u},\mathbf{u}-\mathbf{P}_0\mathbf{u})_{L^2}, \\ &= (\mathbf{u},\mathbf{u}-\widetilde{\mathbf{P}}_0\mathbf{u})_{H_D(\mathbf{curl})} + (1+k^2)(\mathbf{u}-\mathbf{P}_0\mathbf{u},\widetilde{\mathbf{P}}_0\mathbf{u}-\mathbf{P}_0\mathbf{u})_{L^2}, \\ &\leqslant \|\mathbf{u}\|^2_{H_D(\mathbf{curl})} + C_k\frac{h}{p^{1/2-\epsilon}}\|\mathbf{u}-\mathbf{P}_0\mathbf{u}\|^2_{H_D(\mathbf{curl})}. \qquad \square\end{aligned} \tag{2.65}$$

Introducing the error reduction operator $\mathbf{E}^n$ (at step n) associated to the two grid algorithm, i.e., $\mathbf{e}^{(n+1)} = \mathbf{E}^n\mathbf{e}^{(n)}$, we conclude the following theorem:

Theorem 1. *If the coarse grid is fine enough, and*

$$\|\widetilde{\mathbf{E}}^n\mathbf{u}\|_{H_D(\mathbf{curl})} \leqslant \tilde{\delta}\|\mathbf{u}\|_{H_D(\mathbf{curl})} \quad \text{with } 0<\tilde{\delta}<1, \tag{2.66}$$

then

$$\|\mathbf{E}^n\mathbf{u}\|_{H_D(\mathbf{curl})} \leqslant \delta\|\mathbf{u}\|_{H_D(\mathbf{curl})} \quad \text{with } 0<\delta<1, \tag{2.67}$$

where $\delta = \tilde{\delta} + C\max_{l\geqslant 0}\|\mathbf{P}_l - \widetilde{\mathbf{P}}_l\|_{H_D(\mathbf{curl})}$.

The remainder of this section is devoted to proving (2.66), which is a sufficient condition to guarantee the main result (2.67). At this point, we have already determined convergence properties of the two grid solver with respect to the wave number k.

Using standard domain decomposition techniques for SPD problems, it is well-known that (2.66) follows from the following two conditions for the subspace splitting (see, for instance, [28,5], or [26]):

- *Condition I*, necessary to estimate the maximum eigenvalue of the preconditioned matrix:
$$\sum_{i\geqslant 1}\sum_{j\geqslant 1}(\mathbf{q}_i,\mathbf{q}_j)_{H_D(\mathbf{curl})}\leqslant C\left[\sum_{i\geqslant 1}(\mathbf{q}_i,\mathbf{q}_i)_{H_D(\mathbf{curl})}\right]^{1/2}\left[\sum_{j\geqslant 1}(\mathbf{q}_j,\mathbf{q}_j)_{H_D(\mathbf{curl})}\right]^{1/2}, \tag{2.68}$$
where $\mathbf{q}_i \in M_i$. This condition is easily proved by using a coloring algorithm as described, for example, in [26].
- *Condition II*, necessary to estimate the minimum eigenvalue of the preconditioned matrix, by showing that $M=\sum M_l$ is a stable subspace splitting, i.e., for all $\mathbf{q}\in M$, there exist $\mathbf{q}_l\in M_l$ such that $\mathbf{q}=\sum_{l\geqslant 0}\mathbf{q}_l$, and
$$\sum_{l\geqslant 0}\|\mathbf{q}_l\|^2_{H_D(\mathbf{curl})}\leqslant C\|\mathbf{q}\|^2_{H_D(\mathbf{curl})}. \tag{2.69}$$

In order to prove Condition II with a constant independent of h (but possibly dependent upon p), we consider again the discrete Helmholtz decomposition. For all $\mathbf{q}\in(\mathbf{I}-\widetilde{\mathbf{P}}_0)M$:

$$\mathbf{q}=\nabla w+\check{\mathbf{q}}, \tag{2.70}$$

where $\check{\mathbf{q}}\in\check{M}=\{\mathbf{q}\in M:(\mathbf{q},\nabla\phi)_{L^2}=0\ \forall\phi\in W\}$, $w\in W$.

If domain Ω is convex, it is proved in [2] using the fact that $\mathbf{q}\in(\mathbf{I}-\widetilde{\mathbf{P}}_0)M$ that

$$\|\check{\mathbf{q}}\|_{L^2}\leqslant C_p h\|\mathbf{q}\|_{H_D(\mathbf{curl})};\quad \|w\|_{L^2}\leqslant C_p h\|\mathbf{q}\|_{L^2}. \tag{2.71}$$

Assuming that we have an L^2-stable splitting for w (see [2]), and using discrete Poincare and inverse inequalities, we obtain

$$\|\mathbf{q}\|_{L^2}\geqslant C_p h^{-1}\|w\|_{L^2}\geqslant\sum_{l\geqslant 1}C_p h^{-1}\|w_l\|_{L^2}\geqslant\sum_{l\geqslant 1}C_p\|\nabla w_l\|_{L^2}. \tag{2.72}$$

Similarly, assuming that we have an L^2-stable splitting for $\check{\mathbf{q}}$, and using discrete Friedrichs and inverse inequalities, we obtain

$$\|\mathbf{q}\|_{H_D(\mathbf{curl})}\geqslant C_p(1+h^{-1})\|\check{\mathbf{q}}\|_{L^2} \tag{2.73}$$

$$\geqslant\sum_{l\geqslant 1}C_p(1+h^{-1})\|\check{\mathbf{q}}_l\|_{L^2}\geqslant\sum_{l\geqslant 1}C_p\|\check{\mathbf{q}}_l\|_{H_D(\mathbf{curl})}. \tag{2.74}$$

Defining $\mathbf{q}_l=\check{\mathbf{q}}_l+\nabla w_l$, we conclude that for all $\mathbf{q}\in(\mathbf{I}-\widetilde{\mathbf{P}}_0)M$ there exists a decomposition $\mathbf{q}=\sum_{l\geqslant 1}\mathbf{q}_l$ such that

$$\|\mathbf{q}\|^2_{H_D(\mathbf{curl})}\geqslant C_p\sum_{l\geqslant 1}\|\mathbf{q}_l\|^2_{H_D(\mathbf{curl})}. \tag{2.75}$$

Then Condition II holds.

Observation: We have shown that a sufficient condition for convergence of the two grid solver is to have an L^2-stable subspace splittings for *both* parts of the discrete Helmholtz decomposition. In particular:

- $M_l=M_l^v$ (as defined in Section 2.2), implicitly generate L^2-stable splittings for the discrete divergence free and the gradient parts.
- $M_l=M_l^e$ for $1\leqslant l\leqslant N_e, M_l=\nabla W_l^v$ for $N_e+1\leqslant l\leqslant N_e+N_v$ (as defined in Section 2.2), generate L^2-stable splittings for the discrete divergence free (by using the first N_e subspaces) and the gradient parts (by using the last N_v subspaces). Notice that if the last N_v subspaces are not included, then we do *not* obtain a stable splitting for gradients, leading to a diverging two grid algorithm.

- The subspace splitting corresponding to the definition of our smoother $\mathbf{S_E}$ generates a L^2-stable splitting for the discrete divergence free part, while the subspace splitting corresponding to the definition of our smoother $\mathbf{S}_\nabla$ generates a L^2-stable splitting for the gradient part. Thus, we obtain a convergent two grid solver.

Finally, notice that in order to trace the dependence of constants upon p, we cannot use inverse inequalities. Thus, this part of the proof of convergence becomes rather challenging and we have not attempted it. Numerical results indicate that dependence of the two grid solver contraction constant upon p is, at most, logarithmic.

2.5. Stopping criterion

Our ideal stopping criterion translates into condition,

$$\|e^{(n)}\|_B = \|A^{-1}r^{(n)}\|_B \leqslant \epsilon_{\mathrm{TOL}}. \tag{2.76}$$

Obviously, this quantity is not computable, and a stopping criterion can only be based on an approximation to it. In Section 4.2, we derive and analyze numerically two error estimates based on two different approximations to Eq. (2.76), which will be used as two alternative stopping criteria.

3. Implementation

In [25], we discussed several implementation aspects, such as assembling, sparse storage pattern, selection of blocks for the block Jacobi smoother, and construction of the prolongation (restriction) operator for elliptic problems. The first two implementation aspects (assembling and sparse storage pattern) are problem independent, while construction of elliptic operators (stiffness matrix, block Jacobi smoother, and prolongation/restriction operators) can be naturally extended to electromagnetic problems by using $H(\mathbf{curl})$ degrees of freedom (d.o.f.) instead of H^1 d.o.f. Thus, most implementation details discussed in [25] remain valid for EM problems as well.

In this paper, we discuss the implementation of a new embedding operator from gradients of H^1 into $H(\mathbf{curl})$ arising for EM problems. This operator is needed to construct the block Jacobi smoother for gradients.

3.1. The transfer matrix between H^1 and $H(\mathbf{curl})$

We present now shortly the main steps of the algorithm to construct the transfer matrix corresponding to the embedding $\nabla H^1 \subset H(\mathbf{curl})$. More precisely, if $W \subset H^1$ and $M \subset H(\mathbf{curl})$ denote the FE spaces with the corresponding FE basis functions given by $\{e_1,\ldots,e_r\} \in W$, $\{\mathbf{g}_1,\ldots,\mathbf{g}_s\} \in M$, we have

$$w = \sum_{i=1}^{r} w_i e_i \quad \text{and} \quad \mathbf{E} = \sum_{j=1}^{s} E_j \mathbf{g}_j. \tag{3.77}$$

We seek a global matrix T_{ij} such that

$$\nabla e_i = \sum_{j=1}^{s} T_{ji}\mathbf{g}_j, \tag{3.78}$$

which implies the corresponding relation between the H^1- and $H(\mathbf{curl})$-degrees of freedom (d.o.f.),

$$\nabla E_j = \sum_{i=1}^{r} T_{ji} w_i. \tag{3.79}$$

The following algorithm exploits the technology of constrained approximation and generalized connectivities. For an element K, the global basis functions e_i and $\mathbf{g}_j$ are related to the element shape functions ϕ_k and ψ_l,

$$e_i|_K = \sum_k C_{ik}\phi_k, \quad \mathbf{g}_j|_T = \sum_l D_{jl}\psi_l, \tag{3.80}$$

where C_{ik} and D_{ji} are the coefficients corresponding to generalized connectivities related to irregular nodes and the constrained approximation. Formulas (3.80) imply the corresponding relations between local and global d.o.f.

The element transfer matrix S_{ki} relates element shape functions ϕ_k and ψ_l according to the formula

$$\nabla\phi_k = \sum_l S_{lk}\psi_l. \tag{3.81}$$

For the parametric elements forming the de Rham diagram, the element transfer matrix is *independent* of the element, and it can be precomputed for the master element shape functions.

Finally, due to the hierarchical construction of the shape functions, the master element transfer matrix can be precomputed for the maximum order of approximation with the actual element matrix *extracted* from the precomputed one. We use a simple collocation method to precompute S_{kl}.

For an element K, we have

$$\nabla e_i = \sum_j T_{ji}\mathbf{g}_j = \sum_j T_{ji}\sum_l D_{jl}\psi_l \tag{3.82}$$

and, at the same time,

$$\nabla e_i = \sum_k C_{ik}\nabla\phi_k = \sum_k C_{ik}\sum_l S_{lk}\psi_l, \tag{3.83}$$

which implies,

$$\sum_j T_{ji}\sum_l D_{jl} = \sum_k C_{ik}\sum_l S_{lk} \tag{3.84}$$

or

$$\mathbf{D}^{\mathrm{T}}\mathbf{T} = \mathbf{S}^{\mathrm{T}}\mathbf{C}. \tag{3.85}$$

In practice, it is not necessary to invert matrix D^T. This is due to the fact that for each global basis function $\mathbf{g}_j$, there exists at least one element K, for which restriction $\mathbf{g}_j|_K$ reduces to one of the element shape functions, possibly premultiplied with (-1) sign factor. In other words, in the corresponding row in the matrix D_{ji}, there is only one non-zero entry.

The formal algorithm looks as follows:

```
• Initiate $T_{ji} = 0$.
• For each element $K$ in the mesh:
  – For each local $H(\mathbf{curl})$ d.o.f.:
      Exit the cycle if the local d.o.f. is connected to more than one global d.o.f.
      Determine the connected global d.o.f. $j$ and coefficient $D_{jl}$.
      For each local $H^1$ d.o.f. $k$:
          For each connected global $H^1$ d.o.f. $i$ set $T_{ji} = 0$.
```

```
        End of loop through local $H^1$ d.o.f.
        For each local $H^1$ d.o.f. $k$:
            For each connected global $H^1$ d.o.f. $i$ accumulate $T_{ji} = T_{ji} + D_{jk}^{-1} C_{ik} S_{lk}$.
        End of loop through local $H^1$ d.o.f.
    – End of loop through local $H$(curl) d.o.f.
• End of loop through elements.
```

4. Numerical results concerning the two grid solver

This section is devoted to an experimental study of convergence and performance of our two grid solver for EM problems. The study will be based on three model EM problems that we will introduce shortly. Using these examples, we will address the following issues:

- error estimation for the two grid solver,
- the need for controlling gradients by using Hiptmair or AFW decompositions, and,
- the possibility of guiding the optimal *hp*-refinements with a partially converged solution.

4.1. Examples

We shall work with three EM examples. For each model problem, we describe the geometry, governing equations, material coefficients, and boundary conditions. We also display the exact or approximate solution, and we briefly explain the relevance of each problem in this research.

4.1.1. Diffraction of a plane wave on a screen

We consider the problem of a plane wave incident (at a 45° angle) to a diffracting screen.

Geometry. Unit square ($[0,1]^2$). See Fig. 1.

Governing equations. 2D Maxwell's equations.

Material coefficients. Free space.

Boundary conditions. Dirichlet boundary conditions corresponding to the exact solution.

Exact solution. The exact solution can be expressed in terms of Fresnel integrals (see, for example, [9]).

$$H(r,\theta) = \frac{1}{\sqrt{\pi}} \exp^{\pi j/4 - jkr} \{ F[\sqrt{2kr}\sin(\theta/2 - \pi/8)] + F[\sqrt{2kr}\sin(\theta/2 + \pi/8)] \}, \tag{4.86}$$

$$F(u) = \frac{\sqrt{\pi}}{2} \{ \exp^{j\pi/4} - \sqrt{2}[C(\sqrt{2/\pi}u) - jS(\sqrt{2/\pi}u)] \}, \tag{4.87}$$

$$C(z) - jS(z) = \int_0^s \exp^{-1/2\pi j t^2} dt \quad \text{(Fresnel Integrals)}. \tag{4.88}$$

Solution is displayed in Fig. 1.

Observations. Solution of this 2D wave propagation problem in free space lives in $H(\mathbf{curl})$, but not in H^1.

4.1.2. Model waveguide example

Geometry. See Fig. 2.

Governing equations. 2D Maxwell's equations.

Material coefficients. Free space.

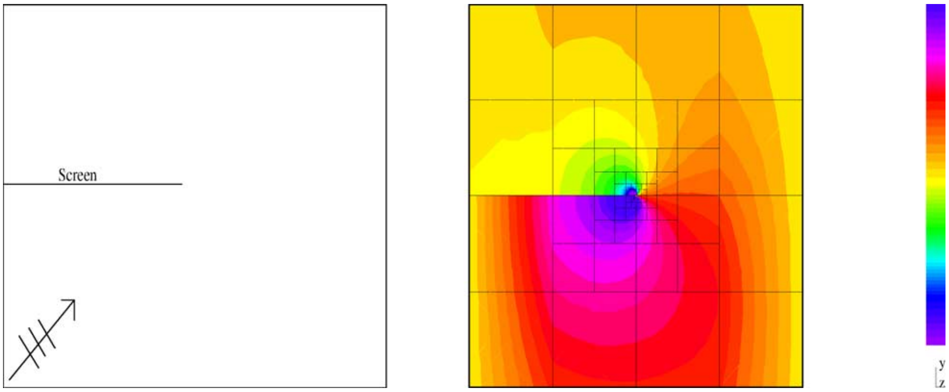

Fig. 1. Geometry and solution (module of the second component of the electric field) of the diffraction of a plane wave on a screen. Different colors correspond to different values of the solution. (For interpretation of the references in figure legends, the reader is referred to the wed version of this article.)

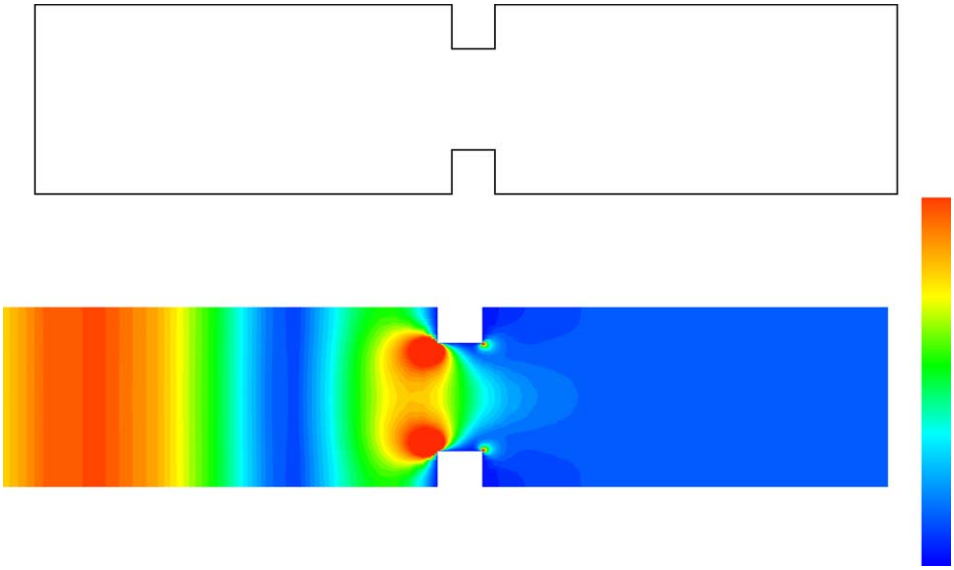

Fig. 2. Geometry and FE solution (module of second component of the magnetic field) of the model waveguide problem. Different colors correspond to different values of the solution, from 0 (blue) to 1 (red).

Boundary conditions. Cauchy boundary condition (to model the left excitation port), absorbing boundary condition (to model the right port) and homogeneous Dirichlet BC (to model the metallic top and bottom walls). See Eqs. (5.105) and (5.106) for details in the Cauchy BC formulation.

Exact solution. The exact solution is unknown. A FE solution is displayed in Fig. 2.

Observations. Solution of this 2D wave propagation problem in free space lives in $H(\mathbf{curl})$, but not in H^1. It involves four singular reentrant corners.

4.1.3. A 3D electromagnetics model problem

Geometry. Unit cube ($[0,1]^3$). See Fig. 3.

Governing equations. Maxwell's equations.

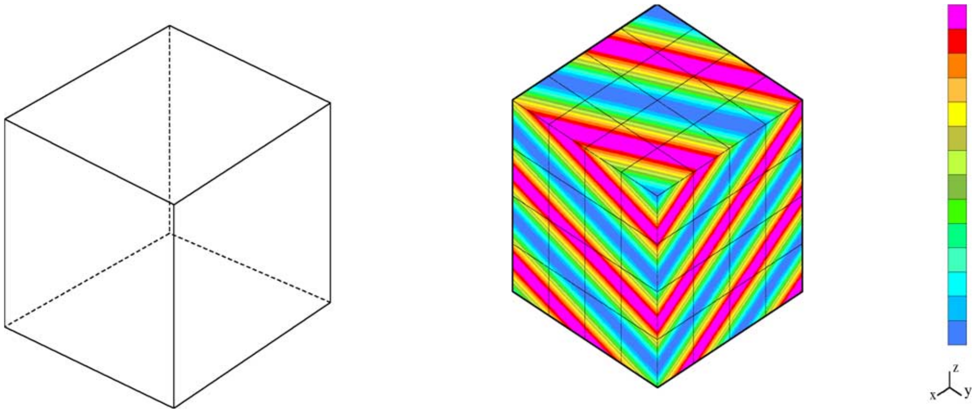

Fig. 3. Geometry and exact solution of the 3D EM model problem with $\mathbf{k} = \frac{0.8\times10^9}{3\times10^8}(\sin(35\pi/180)\cos(25\pi/180)\mathbf{u_x} + \sin(35\pi/180)\times \sin(25\pi/180)\mathbf{u_y} + \cos(35\pi/180))\mathbf{u_z}$. Different colors correspond to different values of the solution, from the minimum (dark blue) to the maximum (pink).

Boundary conditions. Dirichlet at the three faces adjacent to the origin, and Cauchy (impedance) at the remaining three faces.

Exact solution. The plane wave $\boldsymbol{E}(\mathbf{r}) = \mathrm{j}\frac{\mathbf{k}\times\mathbf{p}}{\sqrt{\mathbf{k}\cdot\mathbf{k}}}\exp^{-\mathrm{j}\mathbf{k}\cdot\mathbf{r}}$, where

- $\mathbf{r} = \mathbf{u_x}x + \mathbf{u_y}y + \mathbf{u_z}z$ is the position vector,
- $\mathbf{k} = \mathbf{u_x}k_x + \mathbf{u_y}k_y + u_z k_z$ with k_x, k_y, k_z real indicates the wave amplitude and phase, and,
- $\mathbf{p} = \mathbf{u_x} + \mathbf{u_y} + \mathbf{u_z}$ determines polarization of the plane wave.

Observations. We use the example to study performance of the two grid solver and illustrate necessity (or not) of large order of approximation p for different values of k_x, k_y, and k_z.

4.2. Error estimation

In the following, we focus on error estimation and selection of the stopping criterion discussed in Section 2.5.

First, we consider

$$0.01 \leqslant \frac{\|\alpha^{(n)}S_E r^{(n)}\|_B}{\|\alpha^{(0)}S_E r^{(0)}\|_B} \leqslant 0.1. \tag{4.89}$$

Then, we define two error estimators

$$E^n(1) = \frac{\|\alpha^{(n)}S_E r^{(n)}\|_B}{\|\alpha^{(0)}S_E r^{(0)}\|_B}, \tag{4.90}$$

$$E^n(2) = E^n(1)\frac{\sqrt{1-\left(\frac{g(1)+g(0)}{2}\right)^2}}{\sqrt{1-\left(\frac{g(n)+g(n-1)}{2}\right)^2}}, \tag{4.91}$$

where $g(n) = \frac{E^n(1)}{E^{n-1}(1)}$.

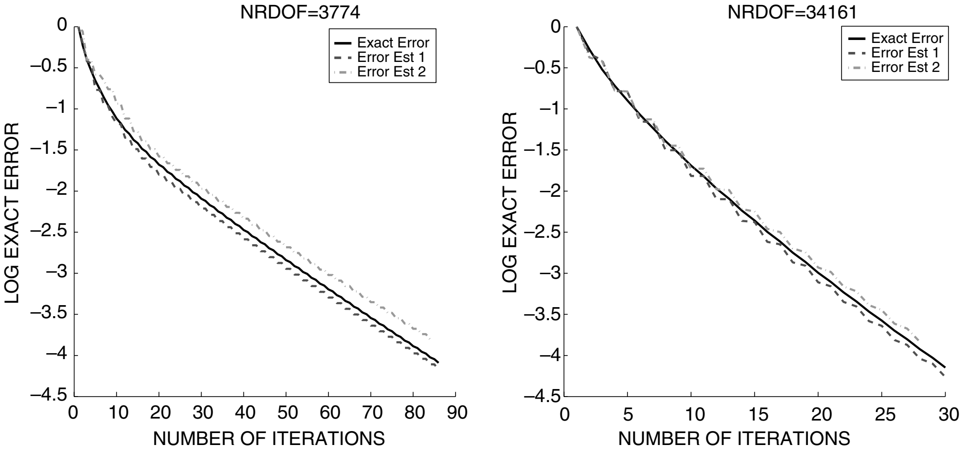

Fig. 4. Model waveguide example. Exact (solid curve) versus two estimated ($E(1)$ and $E(2)$) errors for the two grid solver with a 3774 (left) and 34 161 (right) d.o.f. mesh.

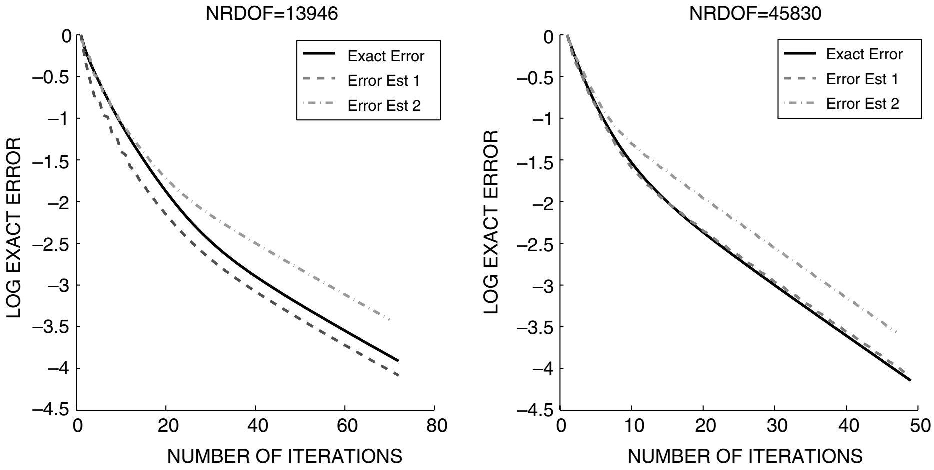

Fig. 5. Diffraction of a plane wave on a screen problem. Exact (solid curve) versus two estimated ($E(1)$ and $E(2)$) errors for the two grid solver with a 13 946 (left) and 45 830 (right) d.o.f. mesh.

Figs. 4 and 5 compare the accuracy of both error estimates ($E^n(1)$ and $E^n(2)$) for different *hp*-grids corresponding to the model waveguide and the diffraction of a plane wave on a screen problems. More numerical results comparing both error estimators can be found in [25]. These results indicate that $E^n(2)$ is a more accurate error estimator than $E^n(1)$ in most (but not all) cases.

4.3. The need for controlling gradients of potentials

In the following, we study numerically the need for using a subspace decomposition for our two grid solver that provides control over gradients, either explicitly (Hiptmair's approach) or implicitly (the AFW approach).

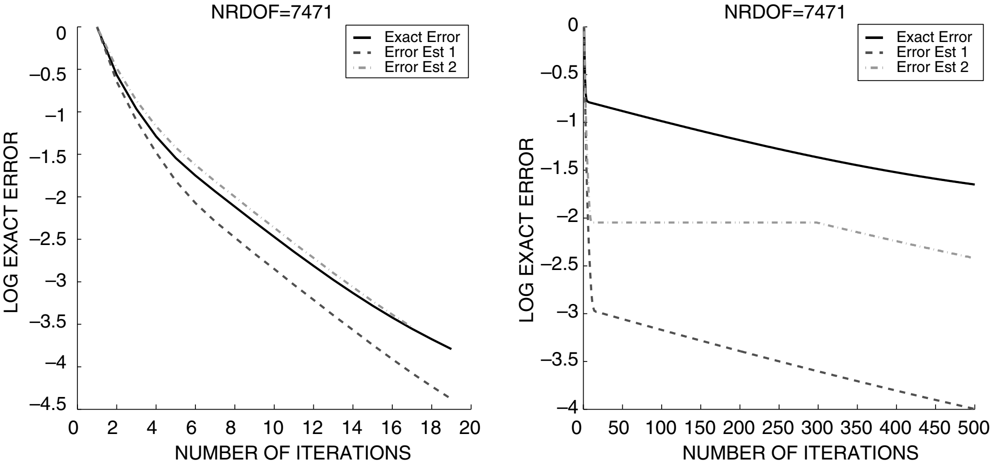

Fig. 6. Diffraction of a plane wave on a screen problem with a purely imaginary wave number (thus, the problem is SPD). Exact (solid curve) versus two estimated ($E(1)$ and $E(2)$) errors for the two grid solver with a 7471 d.o.f. mesh (left figure). In the right figure, correction for gradients were not utilized.

In Fig. 6, we display convergence history for the two grid solver algorithm, with and without the explicit correction for gradients of potentials. If this correction is not included, we may loose control over the kernel of the **curl** operator, leading to a non-converging (or converging very slowly) two grid solver algorithm. Notice that the problem is induced by the presence of the **curl** operator in our variational formulation, and not by the fact that our problem may be indefinite.

In Figs. 7 and 8 we display convergence history for the two grid solver algorithm without the explicit correction for gradients for a 3D EM problem using different smoothers S_1, S_2, and S_3, defined as

- S_1 corresponds to AFW decomposition, that is, a block (of the Jacobi smoother) corresponds to the span of all basis functions whose supports are contained within the support of a vertex basis functions,
- blocks of S_2 correspond to all d.o.f. associated to a particular (modified) element, and
- blocks of S_3 correspond to all d.o.f. associated to all (modified) elements adjacent to a vertex node.

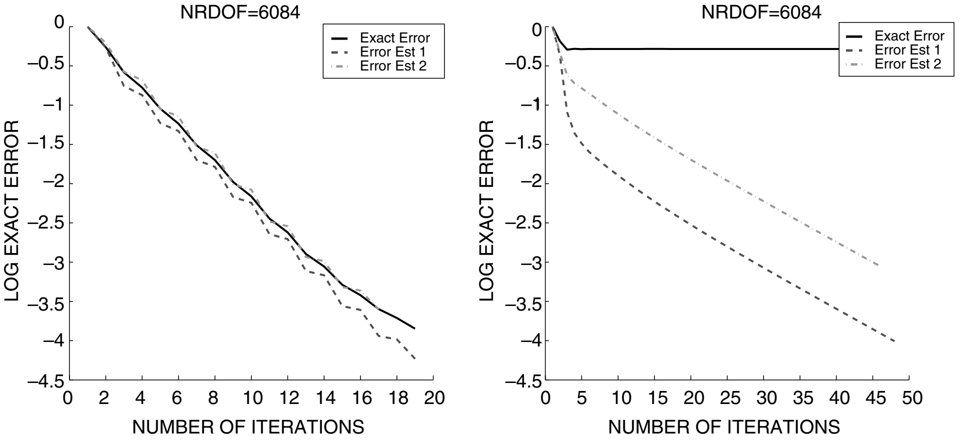

Fig. 7. 3D EM model problem. Exact (solid curve) versus two estimated ($E(1)$ and $E(2)$) errors for the two grid solver with a 6084 d.o.f. mesh (without using an explicit correction for gradients), for smoothers S_1 (left figure) and S_2 (right figure).

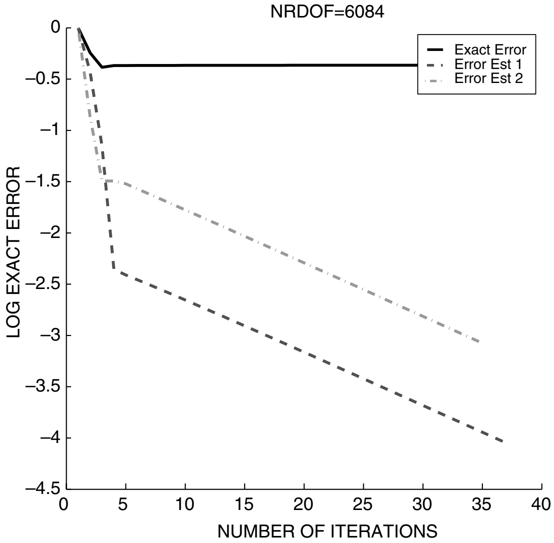

Fig. 8. 3D EM model problem. Exact (solid curve) versus two estimated ($E(1)$ and $E(2)$) errors for the two grid solver with a 6084 d.o.f. mesh (without using an explicit correction for gradients), for smoother S_3.

Although a block of S_3 is larger than the corresponding block of S_1, convergence of the two grid solver is only guaranteed for smoother S_1. Indeed, only S_1 controls the kernel of the **curl** without the need for an explicit gradient correction.

Unfortunately, size of patches associated to block Jacobi smoother S_1 (corresponding to AFW decomposition) are rather large (for $p \gg 1$). Thus, the corresponding two grid solver becomes quite expensive, both, in terms of memory requirements, and CPU time.

4.4. Guiding hp-adaptivity with a partially converged solution

We come now to the most crucial question addressed in this article. For EM problems, how much can we relax our convergence tolerance for the two grid solver, without loosing the exponential convergence in the overall *hp*-adaptive strategy? In the remaining of this section, we try to reach a conclusion via numerical experimentation only.

We work this time with two examples: diffraction of a plane wave on a screen problem, and the model waveguide example. For each of these problems we run the *hp*-adaptive strategy using up to four different strategies to solve the fine grid problem:

(1) a direct (frontal) solver,
(2) the two grid solver with tolerance set to 0.01 (as described in Section 4.2),
(3) the two grid solver with tolerance set to 0.1, and
(4) the two grid solver with tolerance set to 0.3.

As a measure of the error, we use an approximation of the error in $H(\mathbf{curl})$-norm. We simply compute the $H(\mathbf{curl})$-norm of the difference between the coarse and (partially converged) fine mesh solution. The error is reported relative to the norm of the fine grid solution, in percent.

Finally, for each of the cases under study, we report the number of the two grid iterations necessary to achieve the required tolerance.

From Figs. 9 and 10 we draw the following conclusions:

- The two grid solver with 0.01 error tolerance generates a sequence of *hp*-grids that has similar convergence rates to the sequence of *hp*-grids obtained by using a direct solver.
- As we increase the two grid solver error tolerance up to 0.3, the convergence rates of the corresponding sequence of *hp*-grids does not decrease at all. However, the number of iterations (as well as the CPU time) decreases dramatically.
- The number of iterations required by our two grid solver does not increase as the number of degrees of freedom increases.

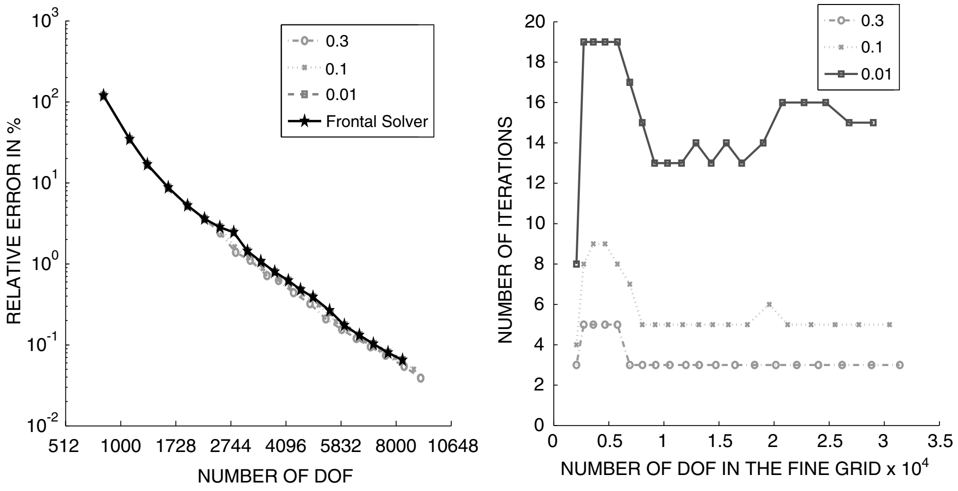

Fig. 9. Diffraction of a plane wave on a screen problem. Guiding *hp*-refinements with a partially converged solution. The left figure displays a discretization error estimate. The right figure shows the number of iterations needed by the two grid solver.

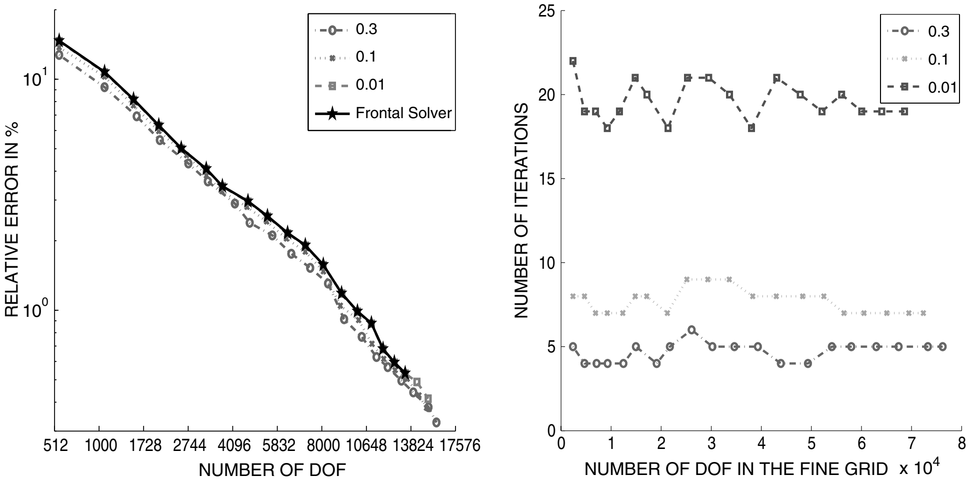

Fig. 10. Model waveguide example. Guiding *hp*-refinements with a partially converged solution. The left figure displays a discretization error estimate. The right figure shows the number of iterations needed by the two grid solver.

To summarize, it looks safe to relax the error tolerance to 0.1 (or even larger) value, without loosing the exponential convergence rates of the overall *hp* mesh optimization procedure.

5. Electromagnetic applications

We conclude our work with a number of more realistic EM examples related to applications in the area of Petroleum Engineering, a simulation of a waveguide filter with six inductive irises, and a dispersion error study in 3D, critical for radar simulations. We focus on advantages and limitations of our numerical technique combining the fully automatic *hp*-adaptive strategy with the two grid solver.

5.1. Modeling of logging while drilling (LWD) EM measuring devices

In this section, we consider two problems posed by the oil company Baker-Atlas[2] in the area of LWD EM measuring devices: an electrostatic edge singularity problem, and an axisymmetric battery antenna problem.

5.1.1. An electrostatic edge singularity problem

A number of LWD instruments incorporate EM antennas covered by metals with plastic apertures. Thus, edge singularities for the electric field may occur on the boundary between plastic and metal.

As a result, to find the electric field near edge singularities may become essential. In addition, edge singularities for the electric (or magnetic) field may occur in the geological formation. Strength of an edge singularity is dependent upon geometry and sources. The fully automatic *hp*-adaptive algorithm does not only detects singularities, but it also distinguishes between singularities of different strength.

Here, we focus on edge singularities arising in electrostatic problems and we present high accuracy approximations for the electric field by considering the following problem with an edge singularity, for which analytical solution is known.

Geometry. See Fig. 11.

Governing equation. Laplace equation ($-\Delta u = 0$).

Boundary conditions. $u = -\ln r$, where $r = \sqrt{(x^2 + y^2)}$.

Exact solution. The analytical solution is known, and it was provided to us by Baker-Atlas[3] (see Eq. (5.98)).

Observations. This 2D problem has a corner singularity located at $(-1, -1)$, which corresponds to an edge singularity in 3D located at $(-1, -1, z)$. We are interested in approximating the exact solution at distances from the singularity 10–12 orders of magnitude smaller than the size of the domain.

To introduce the physics of our problem, we consider two perfect electric conductor (PEC) infinite lines intersecting at a non-zero point (x_c, y_c), as shown in Fig. 1. Let β be the angle between PEC_1 and PEC_2, and ρ a Dirac's delta function distribution of charges concentrated at point $(0,0)$ (Fig. 12).

5.1.1.1. Boundary value problem (BVP). The electrostatic phenomena is governed by the following system of equations:

$$\begin{cases} \nabla \times \boldsymbol{E} = 0, \\ \nabla \cdot (\epsilon \boldsymbol{E}) = \rho. \end{cases} \tag{5.92}$$

---

[2] Baker-Atlas, a division of Baker-Hughes.

[3] We thank Lev Tabarovsky and Alex Bespalov for this example.

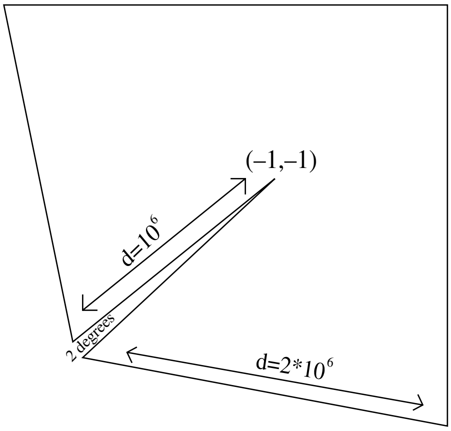

Fig. 11. Geometry of the electrostatic problem with an edge singularity.

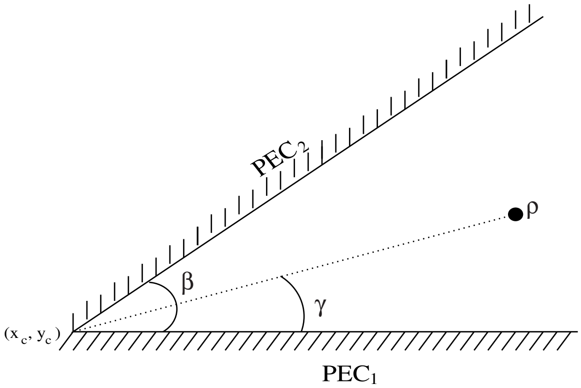

Fig. 12. Model problem.

Thus, solving for scalar potential p, we obtain

$$\mathrm{div}\nabla p = \Delta p = \frac{\rho}{\epsilon} \tag{5.93}$$

with boundary conditions:

- $p = 0$ on PEC_1 and PEC_2.
- $p = 0$ on a boundary far enough from the source. Since electric field $\boldsymbol{E}$ decays as $1/r$ (where r is the distance from a given point to the source), for r large enough (for example, $r = 10^6$), the electric field intensity is negligible, and can be replaced by 0.

Thus, denoting by Ω our computational domain (shown in Fig. 11) and by Γ its boundary, we obtain

$$\begin{cases} \Delta p = \dfrac{\rho}{\epsilon} & \text{in } \Omega, \\ p = 0 & \text{on } \Gamma. \end{cases} \tag{5.94}$$

5.1.1.2. Secondary (scattered) field. Now, let ρ be a unitary electric charge distribution concentrated at the origin in free space. Solution is given by $p^{\mathrm{prim}} = \ln r$. Then

$$\begin{cases} \Delta p - p^{\mathrm{prim}} = 0 & \text{in } \Omega, \\ p - p^{\mathrm{prim}} = 0 - \ln r = -\ln r & \text{on } \Gamma. \end{cases} \tag{5.95}$$

Solving the problem for secondary potential $p^{\mathrm{sec}} = p - p^{\mathrm{prim}}$, we avoid modeling of the source, obtaining:

$$\begin{cases} \Delta p^{\mathrm{sec}} = 0 & \text{in } \Omega, \\ p^{\mathrm{sec}} = -\ln r & \text{on } \Gamma. \end{cases} \tag{5.96}$$

5.1.1.3. Variational formulation. In order to derive the corresponding variational formulation, we multiply equation $\Delta p^{\mathrm{sec}} = 0$ by a test function $v \in V = H_0^1(\Omega) = \{u \in H^1(\Omega) : u = 0 \text{ on } \Gamma\}$, and integrate (by parts) over domain Ω. We obtain

$$\begin{cases} \text{Find } u \in u_0 + V, \\ \displaystyle\int_{\Omega} \nabla u \nabla v = 0 \quad \forall v \in V, \end{cases} \tag{5.97}$$

where u_0 is a lift corresponding to the non-homogeneous Dirichlet boundary conditions.

5.1.1.4. Exact solution. The exact solution of this electrostatic problem can be computed analytically [22]. At points located on the surface of PEC_1, the normal component of the electric field as a function of β, γ, x, y, x_c, and y_c, is given by

$$E_n = -\frac{2\pi}{s} \frac{l^{\frac{\pi}{\beta}} \sin\left(\frac{\pi\gamma}{\beta}\right)}{\left[1 - 2l^{\frac{\pi}{\beta}} \cos\left(\frac{\pi\gamma}{\beta}\right) + l^{\frac{2\pi}{\beta}}\right]}, \tag{5.98}$$

where s is the distance from a given point (x, y) to the corner (x_c, y_c), i.e.,

$$s = \sqrt{(x - x_c)^2 + (y - y_c)^2} \tag{5.99}$$

and l is given by

$$l = \frac{\sqrt{x_c^2 + y_c^2}}{s}. \tag{5.100}$$

In particular, for $\gamma = \frac{\beta}{2}$, we have

$$E_n = -\frac{2\pi}{\sqrt{x_c^2 + y_c^2}} \frac{1}{\left[l^{-1-\frac{\pi}{\beta}} + l^{-1+\frac{\pi}{\beta}}\right]} = \frac{-2\pi}{\left[(x_c^2 + y_c^2)^{-\frac{\pi}{2\beta}} s^{1+\frac{\pi}{\beta}} + (x_c^2 + y_c^2)^{\frac{\pi}{2\beta}} s^{1-\frac{\pi}{\beta}}\right]}. \tag{5.101}$$

There exists a singularity at point (x_c, y_c) (edge singularity in three dimensions) if and only if $\pi < \beta$. Furthermore, the larger is β the stronger is the singularity. In particular, the strength of singularity is independent of the selected non-zero point (x_c, y_c). Therefore, we set $x_c = y_c = -1$, obtaining:

$$E_n = E_n(s, \beta) = \frac{-2\pi}{\left[2^{-\frac{\pi}{2\beta}} s^{1+\frac{\pi}{\beta}} + 2^{\frac{\pi}{2\beta}} s^{1-\frac{\pi}{\beta}}\right]}. \tag{5.102}$$

For simplicity, we will restrict ourselves only to the case $\beta = 358°$, which corresponds to a strong edge singularity.

5.1.1.5. Numerical results. Figs. 13–19, show different zooms on the final *hp*-grid (generated automatically by our refinement strategy) toward the singularity. Notice that elements near the singularity are up to thirteen orders of magnitude smaller than other elements in the same grid!

Finally, in Fig. 20, a comparison between the exact and approximate solutions of the normal component of the electric field over PEC_1 at points located near the singularity is displayed. Notice that in order to study behavior of the edge singularity, we are interested in points located at distances 10^{-6}–10^{-2} from the singularity. As it can be concluded from Fig. 20, we do fully resolve the problem in the region of interest.

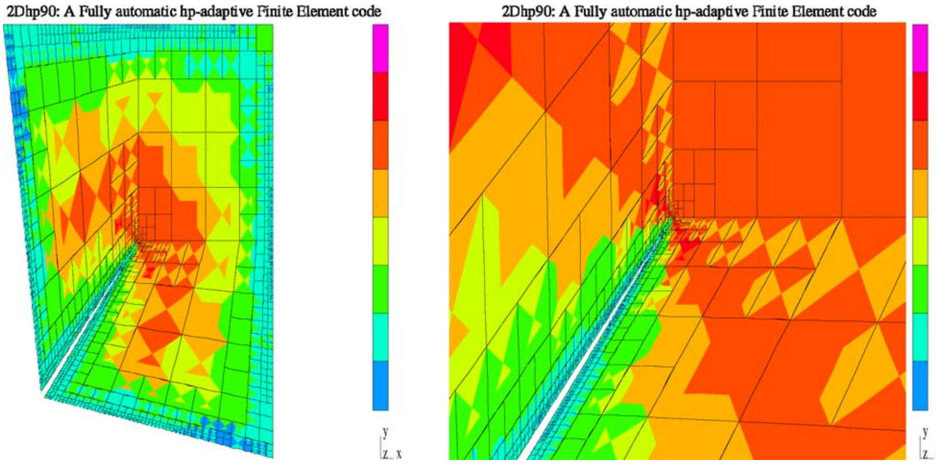

Fig. 13. Final *hp*-grid (zooms = 1, 10) for the electrostatic edge singularity problem. Different colors indicate different polynomial orders of a approximation, from $p = 1$ (dark blue) to $p = 8$ (pink).

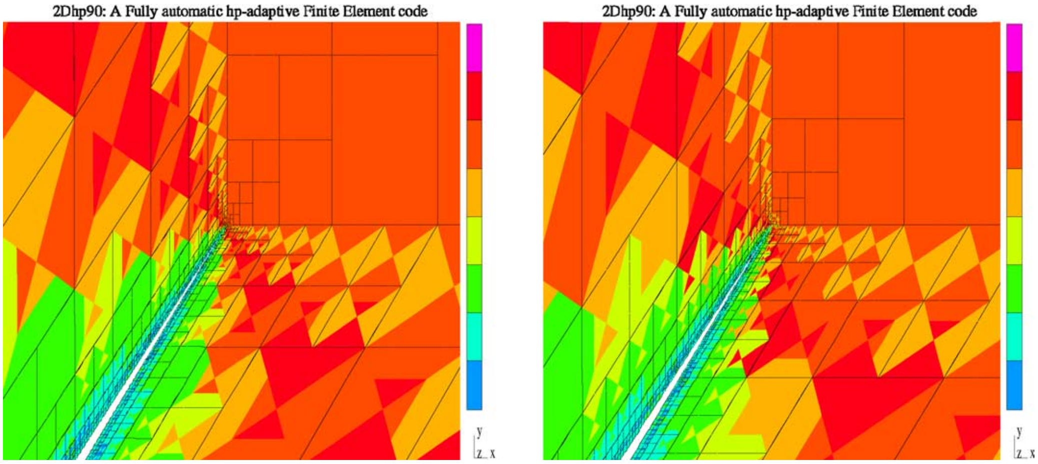

Fig. 14. Final *hp*-grid (zooms = $10^2, 10^3$) for the electrostatic edge singularity problem. Different colors indicate different polynomial orders of a approximation, from $p = 1$ (dark blue) to $p = 8$ (pink).

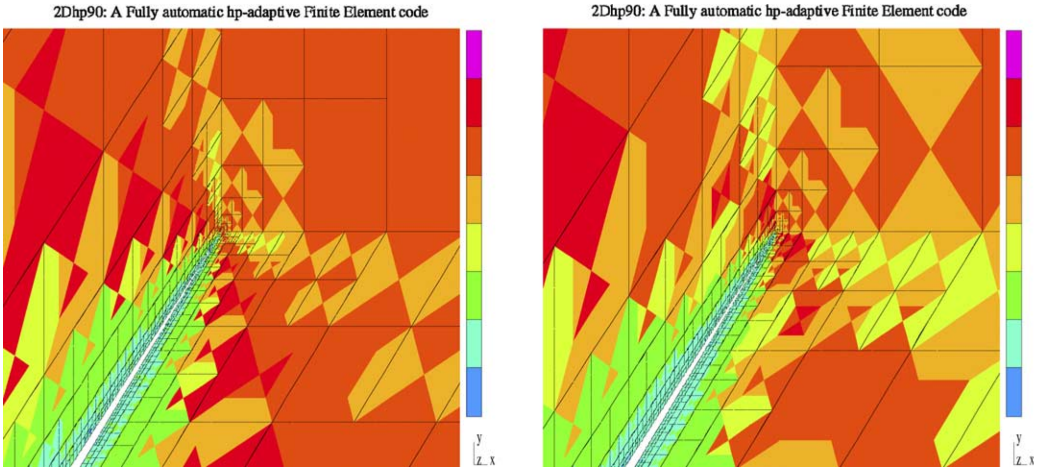

Fig. 15. Final *hp*-grid (zooms = $10^4, 10^5$) for the electrostatic edge singularity problem. Different colors indicate different polynomial orders of a approximation, from $p = 1$ (dark blue) to $p = 8$ (pink).

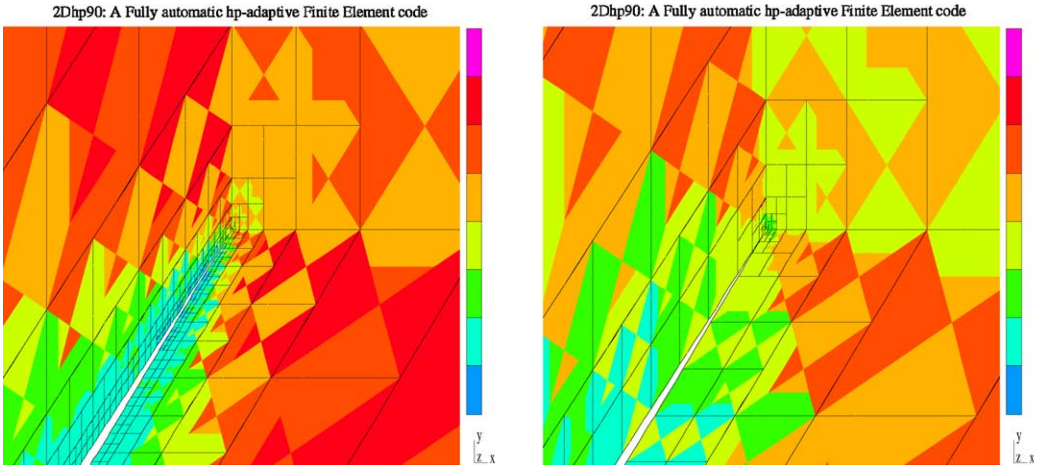

Fig. 16. Final *hp*-grid (zooms = $10^6, 10^7$) for the electrostatic edge singularity problem. Different colors indicate different polynomial orders of a approximation, from $p = 1$ (dark blue) to $p = 8$ (pink).

5.1.2. An axisymmetric battery antenna problem: the need for goal-oriented adaptivity

We consider the following axisymmetric battery antenna in a homogeneous medium with non-zero conductivity σ.

Geometry. 3D axisymmetric problem. See Fig. 21.

Governing equations. Axisymmetric 3D Maxwell's equations.

Material coefficients.

- Conductivity: 1 S.
- Frequency: 1 MHz.
- Relative permeability and permittivity: 1.

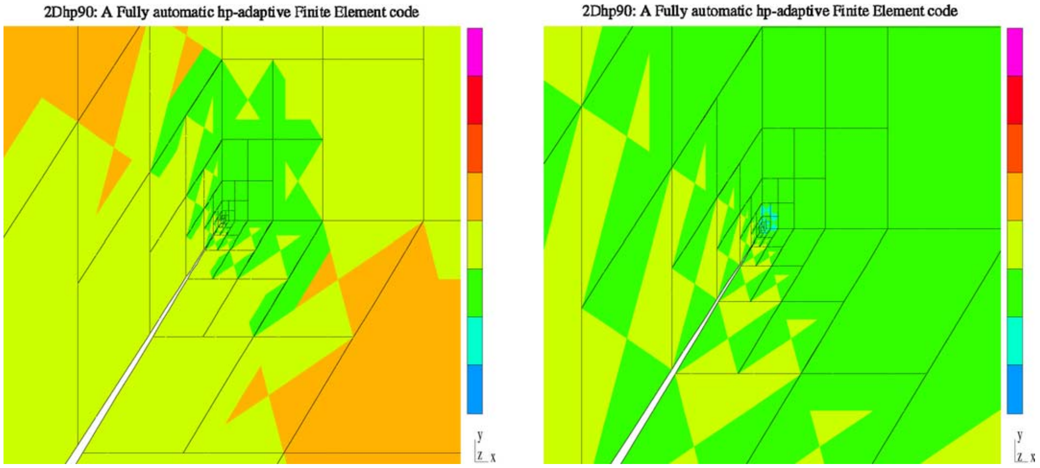

Fig. 17. Final *hp*-grid (zooms = $10^8, 10^9$) for the electrostatic edge singularity problem. Different colors indicate different polynomial orders of a approximation, from $p = 1$ (dark blue) to $p = 8$ (pink).

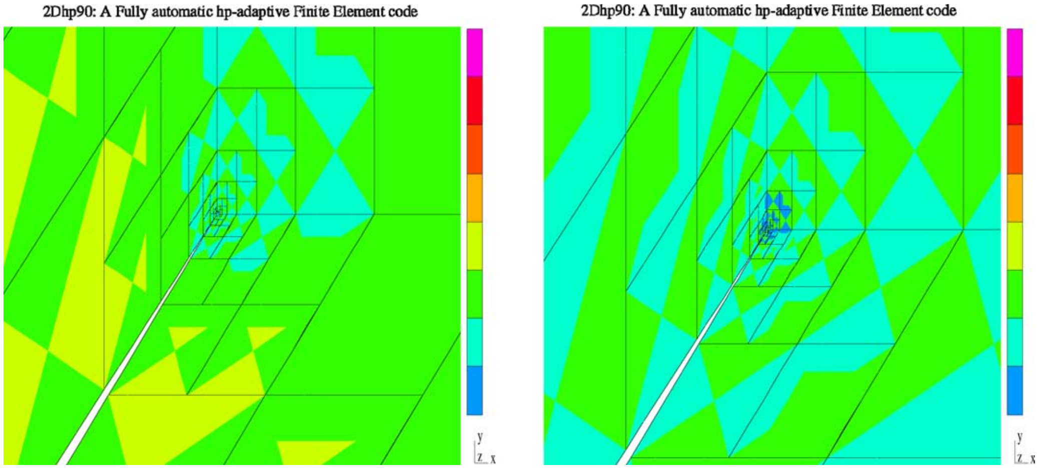

Fig. 18. Final *hp*-grid (zooms = $10^{10}, 10^{11}$) for the electrostatic edge singularity problem. Different colors indicate different polynomial orders of a approximation, from $p = 1$ (dark blue) to $p = 8$ (pink).

Boundary conditions. Homogeneous Dirichlet and Neumann, see Eq. (5.103).

Exact solution. The analytical solution is unknown, although it is known to decay exponentially as we go away from the battery antenna, since we have a non-zero conductivity.

Observations. We are interested in approximating the exact solution at points far away (0.5 m) from the antenna.

The original 3D problem can be reduced to a 2D boundary value problem, which can be formulated in terms of a 2D *E*-field obtained by solving the reduced wave equation with the appropriate boundary conditions.

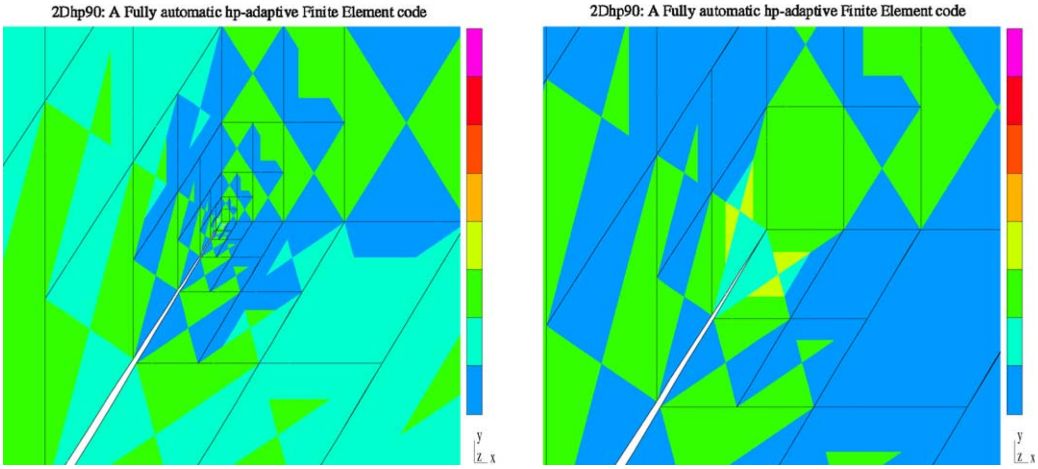

Fig. 19. Final *hp*-grid (zooms $= 10^{12}, 10^{13}$) for the electrostatic edge singularity problem. Different colors indicate different polynomial orders of a approximation, from $p = 1$ (dark blue) to $p = 8$ (pink).

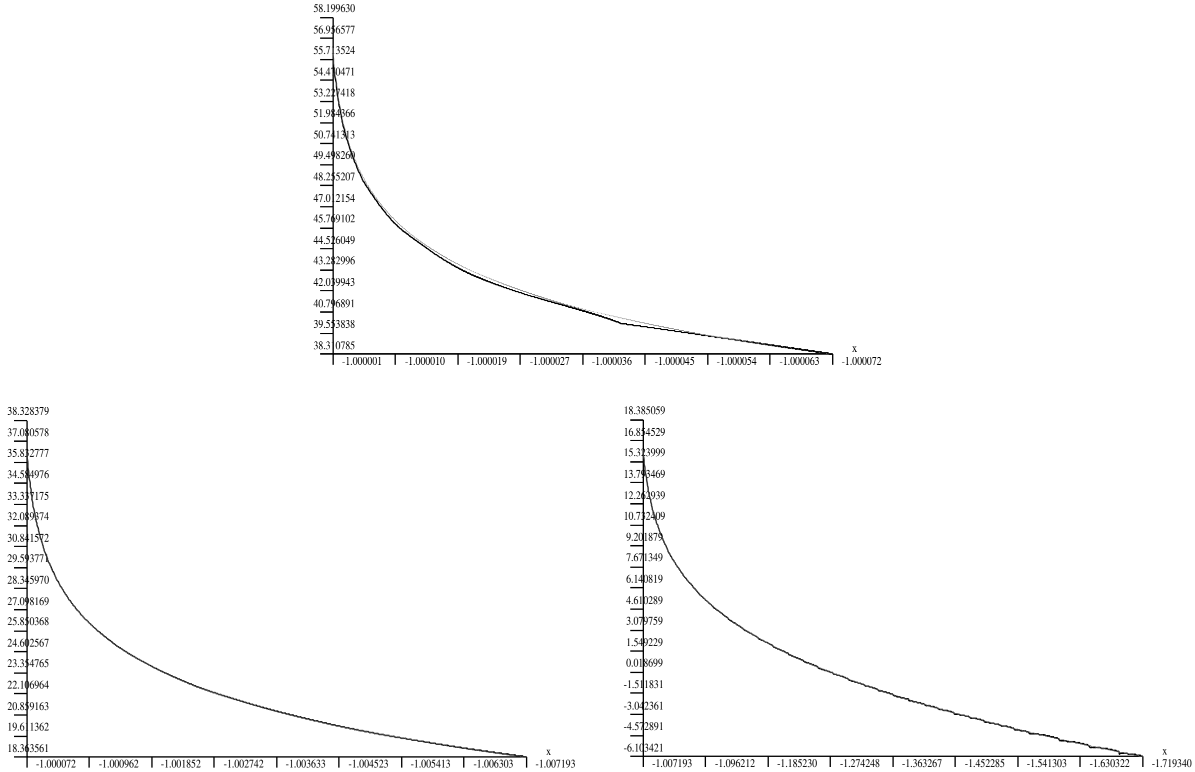

Fig. 20. Value on the PEC_1 edge of normal component of electric field at distances 10^{-6}–10^{-4} (top figure), 10^{-4}–10^{-2} (bottom left figure), and 10^{-2}–10^{0} (bottom right figure) from the singularity. The dotted curve denotes exact solution, while FE approximation is represented by a solid curve.

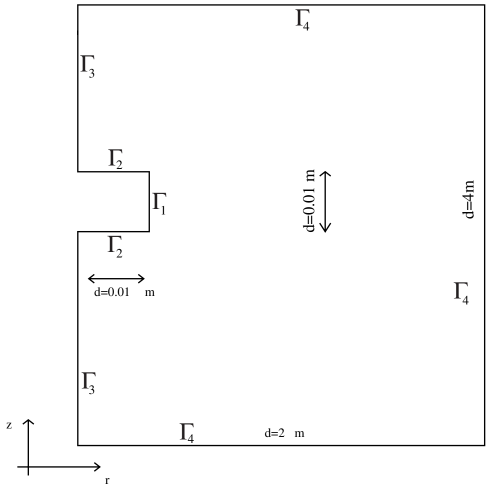

Fig. 21. A 2D cross section geometry of the axisymmetric battery antenna problem.

Since $\sigma \neq 0$, it is known that the electric field intensity decays exponentially as we move away from the source (battery antenna), and we can select a finite computational domain with homogeneous Dirichlet boundary conditions enforced at points distant from the antenna. More precisely, we may formulate our boundary value problem in domain Ω (shown in Fig. 21) as follows:

$$\begin{cases} \nabla \times \left(\dfrac{1}{\mu} \nabla \times \boldsymbol{E} \right) - (\omega^2 \epsilon - \mathrm{j}\omega\sigma)\boldsymbol{E} = 0 & \text{in } \Omega, \\ \mathbf{n} \times \nabla \times \boldsymbol{E} = -\mathrm{j}\omega\mu & \text{on } \Gamma_1, \\ \mathbf{n} \times \nabla \times \boldsymbol{E} = 0 & \text{on } \Gamma_3, \\ \mathbf{n} \times \boldsymbol{E} = 0 & \text{on } \Gamma_2 \cup \Gamma_4. \end{cases} \tag{5.103}$$

The corresponding variational formulation is given by

$$\begin{cases} \text{Find } \boldsymbol{E} \in H_D(\mathbf{curl}; \Omega) \text{ such that} \\ \displaystyle\int_\Omega \frac{1}{\mu} (\nabla \times \boldsymbol{E}) \cdot (\nabla \times \bar{\boldsymbol{F}}) \, \mathrm{d}x - \int_\Omega (\omega^2 \epsilon - \mathrm{j}\omega\sigma) \boldsymbol{E} \cdot \bar{\boldsymbol{F}} \, \mathrm{d}x \\ \quad = \omega^2 \mu \left\{ \displaystyle\int_{\Gamma_1} \bar{\boldsymbol{F}} \, \mathrm{d}S \right\} \quad \text{for all } \boldsymbol{F} \in H_D(\mathbf{curl}; \Omega), \end{cases} \tag{5.104}$$

where $H_D(\mathbf{curl};\Omega) = \{\boldsymbol{E} \in H(\mathbf{curl};\Omega) : \mathbf{n} \times \boldsymbol{E}|_{(\Gamma_2 \cup \Gamma_4)} = 0\}$ is the Hilbert space of *admissible solutions*.

The corresponding stabilized variational formulation can then be derived using techniques of Section 2.1.

Fig. 22 shows convergence history for a sequence of optimal *hp*-grids produced by our refinement strategy, which is delivering exponential convergence rates.

The final *hp*-grid (with the corresponding zooms toward the battery antenna) is displayed in Figs. 23–27. This final *hp*-grid is optimal in the sense that it minimizes the relative energy norm error with respect to the number of unknowns.

Unfortunately, the objective of this problem is to estimate the electric field at distances far away from the source. And for this purpose, an energy norm based refinement strategy is not suitable, and a goal-oriented adaptive strategy is needed.

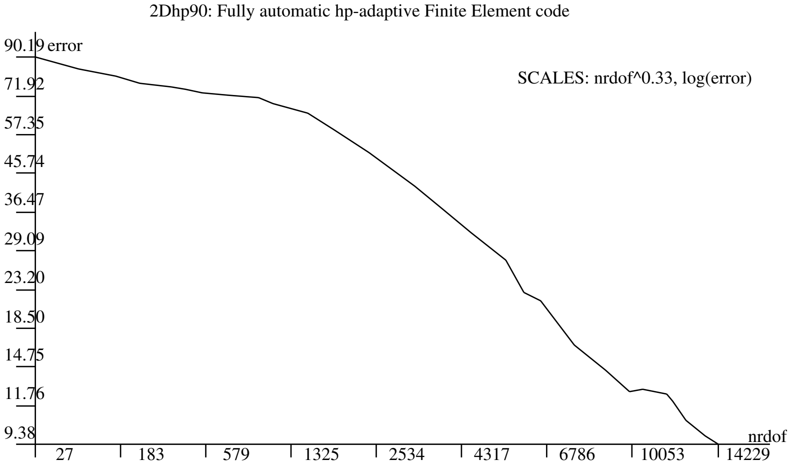

Fig. 22. Convergence history of the axisymmetric battery antenna in the scales number of unknowns to the power of 1/3 (algebraic scale) vs logarithm of the relative energy norm error.

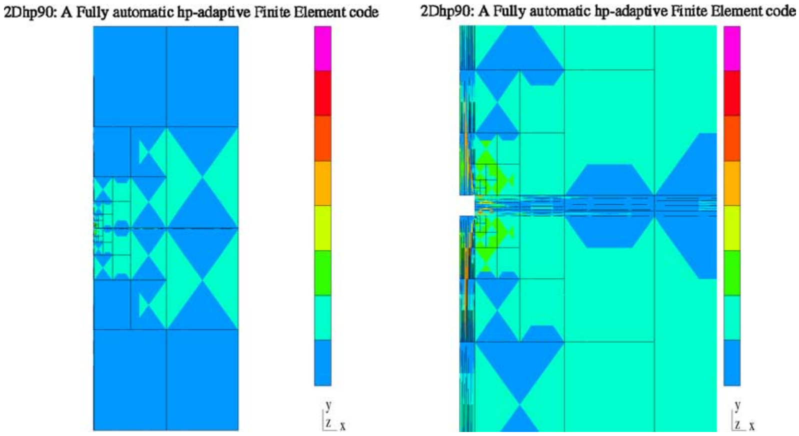

Fig. 23. Final *hp*-grid (zooms = 1, 10) for the axisymmetric battery antenna problem. Different colors indicate different polynomial orders of a approximation, from $p = 1$ (dark blue) to $p = 8$ (pink).

5.2. Waveguide design

In this section, we focus our attention on the following six inductive irises waveguide problem:
Geometry. A six inductive irises filter[4] of dimensions ≈20 × 2 × 1 cm. For details, see Fig. 28.
Governing equations. Maxwell's equations.
Material coefficients.

- Free space.
- Operating Frequency ≈ 8.8–9.6 GHz.
- Cutoff frequency ≈ 6.56 GHz.

---

[4] We thank Dr. Luis Garcia-Castillo and Mr. Sergio Llorente for this problem.

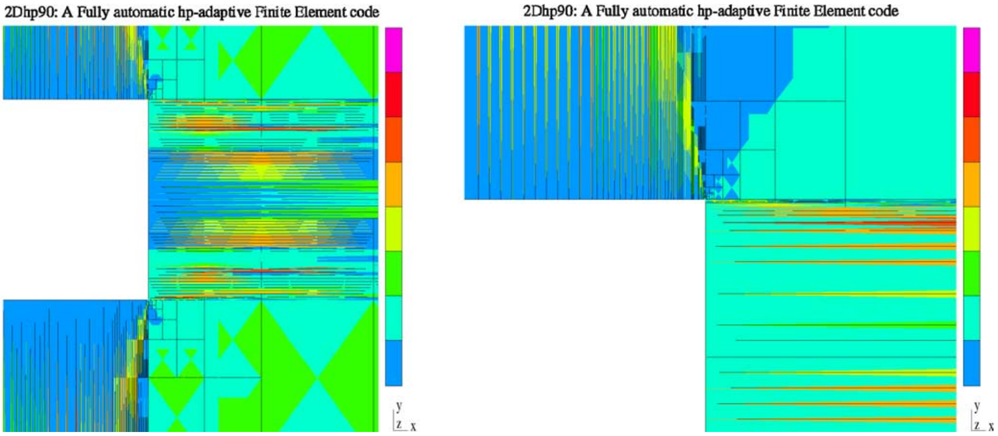

Fig. 24. Final *hp*-grid (zooms $= 10^2, 10^3$) for the axisymmetric battery antenna problem. Different colors indicate different polynomial orders of a approximation, from $p = 1$ (dark blue) to $p = 8$ (pink).

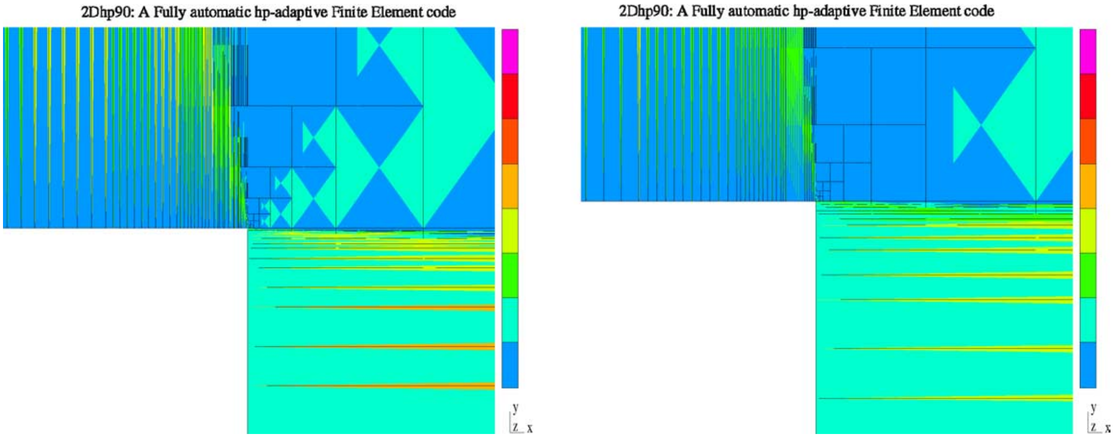

Fig. 25. Final *hp*-grid (zooms $= 10^4, 10^5$) for the axisymmetric battery antenna problem. Different colors indicate different polynomial orders of a approximation, from $p = 1$ (dark blue) to $p = 8$ (pink).

Boundary conditions. Dirichlet, Neumann and Cauchy, see Eq. (5.105).
Exact solution. The exact solution is unknown. A FE solution is displayed in Fig. 28.
Observations.

- H-plane six inductive irises filter.
- Solution of this wave propagation problem lives in $H(\mathbf{curl})$, but not in H^1.
- Solution involves resolution of 24 singular reentrant corners.
- Dominant mode (source): TE_{10}-mode.

First, we formulate the boundary value problem. Next, we present the variational formulation and discuss a way to compute the scattering parameters, the primary quantity of interest for the waveguide design. Third, we display results obtained with our numerical method. Finally, we use the problem to illustrate some of the limitations of the fully automatic *hp*-adaptive strategy, and the two grid solver.

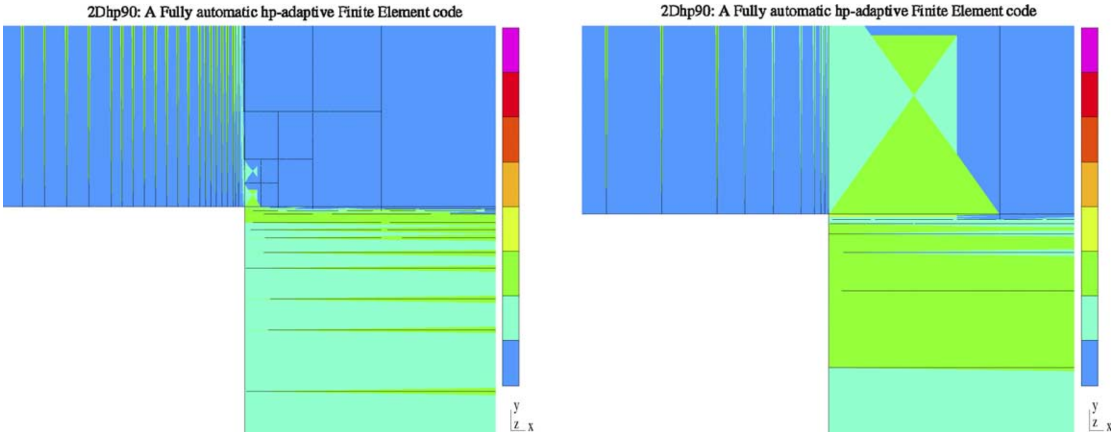

Fig. 26. Final *hp*-grid (zooms = $10^6, 10^7$) for the axisymmetric battery antenna problem. Different colors indicate different polynomial orders of a approximation, from $p = 1$ (dark blue) to $p = 8$ (pink).

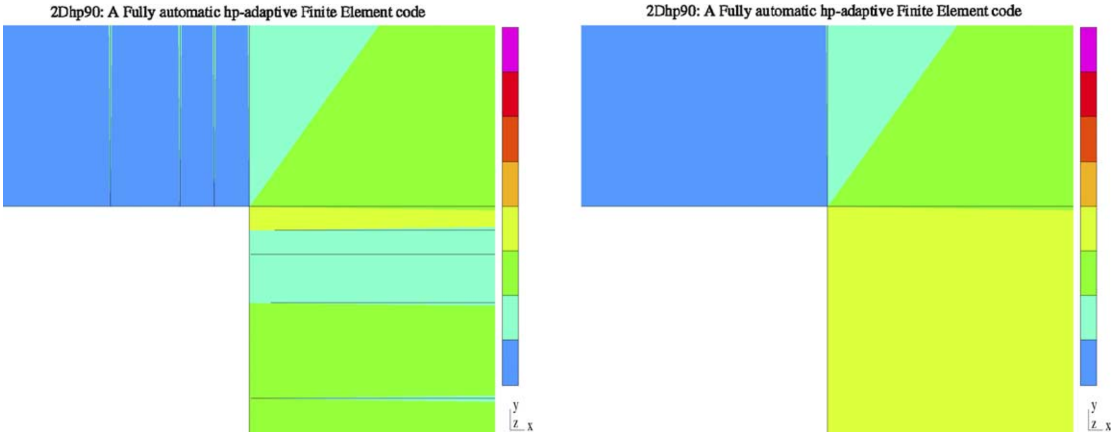

Fig. 27. Final *hp*-grid (zooms = $10^8, 10^9$) for the axisymmetric battery antenna problem. Different colors indicate different polynomial orders of a approximation, from $p = 1$ (dark blue) to $p = 8$ (pink).

5.2.1. Formulation

We excite the TE_{10}-mode at the left-hand side port of the waveguide structure (see Fig. 28), and we consider an H-plane discontinuity, i.e., the magnetic field is invariant with respect to the *z*-direction. Thus, our original 3D problem can be reduced to a 2D boundary value problem, which we can formulate in terms of the 2D *H*-field as follows:

$$\begin{cases} \nabla \times \left(\frac{1}{\epsilon}\nabla \times \boldsymbol{H}\right) - \omega^2\mu\boldsymbol{H} = 0 & \text{in } \Omega, \\ \mathbf{n} \times \frac{1}{\epsilon}\nabla \times \boldsymbol{H} = \frac{j\omega^2\mu}{\beta_{10}}\mathbf{n} \times \mathbf{n} \times (2\boldsymbol{H}^{\text{inc}} - \boldsymbol{H}) & \text{on } \Gamma_1, \\ \mathbf{n} \times \frac{1}{\epsilon}\nabla \times \boldsymbol{H} = -\frac{j\omega^2\mu}{\beta_{10}}\mathbf{n} \times \mathbf{n} \times \boldsymbol{H} & \text{on } \Gamma_2, \\ \mathbf{n} \times \frac{1}{\epsilon}\nabla \times \boldsymbol{H} = \mathbf{0} & \text{on } \Gamma_3, \end{cases} \tag{5.105}$$

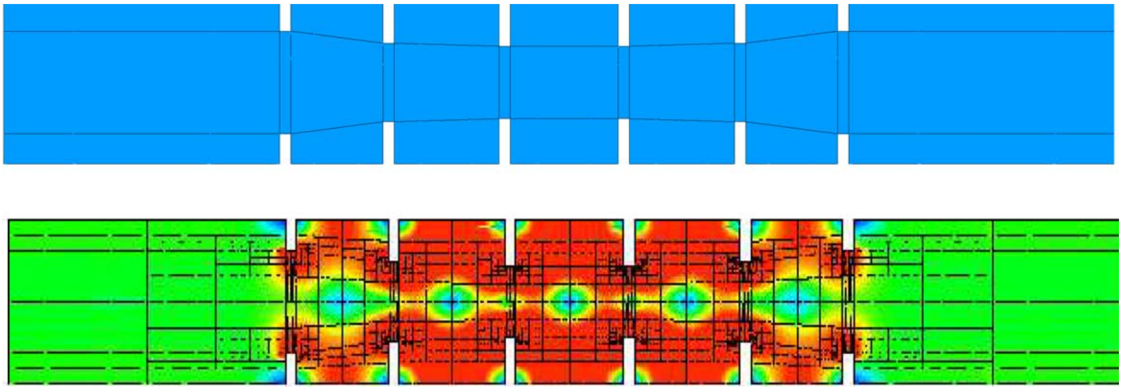

Fig. 28. Geometry and FE solution ($\sqrt{|H_x|^2 + |H_y|^2}$) at 8.82 GHz of the waveguide problem with six inductive irises. Different colors correspond to different values of the solution, from 0 (blue) to 1 (red).

where Γ_1, Γ_2, and Γ_3 are the parts of the boundary corresponding to the excitation port (left port), non-excitation port (right port), and the perfect electric conductor respectively; β_{10} refers to the propagation constant of the TE_{10} mode; and $\boldsymbol{H}^{\text{inc}}$ is the incident magnetic field at the excitation port.

The corresponding variational formulation is given by

$$\left\{\begin{array}{l} \text{Find } \boldsymbol{H} \in H_D(\mathbf{curl};\Omega) \text{ such that} \\ \displaystyle\int_\Omega \frac{1}{\epsilon}(\boldsymbol{\nabla}\times\boldsymbol{H})\cdot(\boldsymbol{\nabla}\times\bar{\boldsymbol{F}})\,\mathrm{d}x - \int_\Omega \omega^2\mu\boldsymbol{H}\cdot\bar{\boldsymbol{F}}\,\mathrm{d}x \\ \displaystyle\quad +\frac{\mathrm{j}\omega^2\mu}{\beta_{10}}\int_{\Gamma_1\cup\Gamma_2}(\mathbf{n}\times\boldsymbol{H})\cdot(\mathbf{n}\times\bar{\boldsymbol{F}})\,\mathrm{d}S \\ \displaystyle\quad = 2\frac{\mathrm{j}\omega^2\mu}{\beta_{10}}\int_{\Gamma_1}(\mathbf{n}\times\boldsymbol{H}^{\text{inc}})\cdot(\mathbf{n}\times\bar{\boldsymbol{F}})\,\mathrm{d}S \quad \text{for all } \boldsymbol{F}\in H_D(\mathbf{curl};\Omega). \end{array}\right. \tag{5.106}$$

In the above $H_D(\mathbf{curl};\Omega)$ is the *space of admissible solutions*,

$$\boldsymbol{H}_D(\mathbf{curl};\Omega) := \{\boldsymbol{H}\in\boldsymbol{L}^2(\Omega) : \boldsymbol{\nabla}\times\boldsymbol{H}\in\boldsymbol{L}^2(\Omega)\}. \tag{5.107}$$

The stabilized variational formulation can be derived using techniques of Section 2.1.

5.2.2. Scattering parameters

The objective of the waveguide problem is to compute the so called scattering parameters. Since the only propagating mode is TE_{10}, we have two *power waves*[5] present at each port Γ_i ($i = 1, 2$): one going inward (a_i), and other going outward (b_i) the structure. The relation between the power waves is linear, and may be written in matrix form as

$$\begin{pmatrix} b_1 \\ b_2 \end{pmatrix} = \begin{pmatrix} S_{11} & S_{12} \\ S_{21} & S_{22} \end{pmatrix} \cdot \begin{pmatrix} a_1 \\ a_2 \end{pmatrix}, \tag{5.108}$$

where S_{ij} are the scattering parameters, or simply S parameters. Thus, the S parameters relate the incident and reflected power waves. Note that S_{11}, S_{22} are *reflection* coefficients and S_{12}, S_{21} are *transmission* coefficients.

---

[5] A power wave can be identified with a complex number such that its magnitude squared represents the power carried by the wave, and its argument is the phase of the wave.

Table 1
Convergence (or not) of the two grid solver for different quasi-uniform initial grids

Does the two grid solver converge?	$p = 1$	$p = 2$	$p = 3$	$p = 4$
Number of elements per $\lambda = 7$, 13	Yes	Yes	Yes	Yes
Number of elements per $\lambda = 7$, 11	No	No	No	Yes
Number of elements per $\lambda = 6$, 13	No	No	No	No

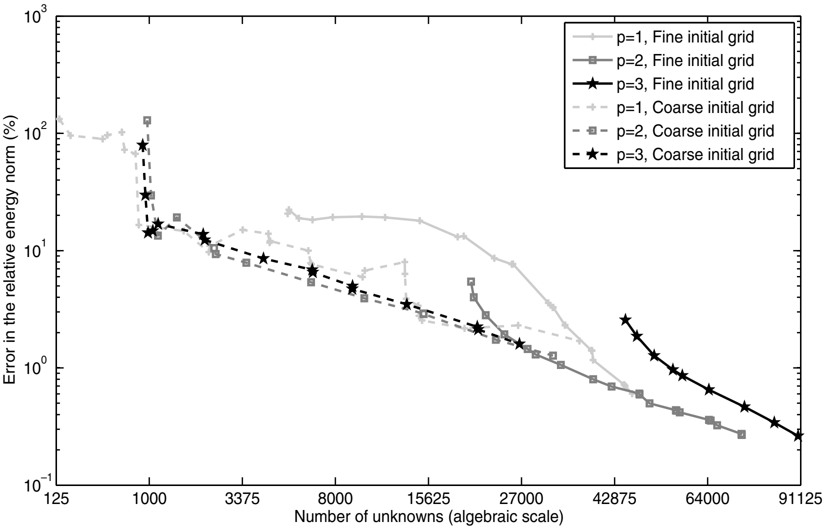

Fig. 29. Convergence history using the fully automatic *hp*-adaptive strategy for different initial grids. Different grey-scale colors correspond to different initial orders of approximation. Twenty-seven is the minimum number of elements needed to reproduce the geometry, while 1620 is the minimum number of elements needed to reproduce the geometry and to guarantee convergence of the two grid solver.

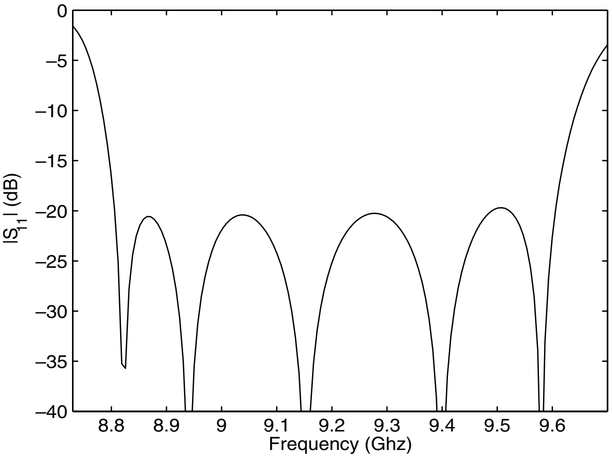

Fig. 30. Return loss of the waveguide structure.

The absorbing boundary condition at Γ_2 implies $a_2 = 0$, and (5.108) reduces to

$$S_{11} = \frac{b_1}{a_1}; \quad S_{12} = \frac{b_2}{a_1}. \tag{5.109}$$

Also, we have the reciprocity condition, given by $S_{12} = S_{21}$ (see [17]). And since no losses occur within the waveguide structure, symmetry property $|S_{11}|^2 + |S_{22}|^2 = 1$ holds (see [18]).

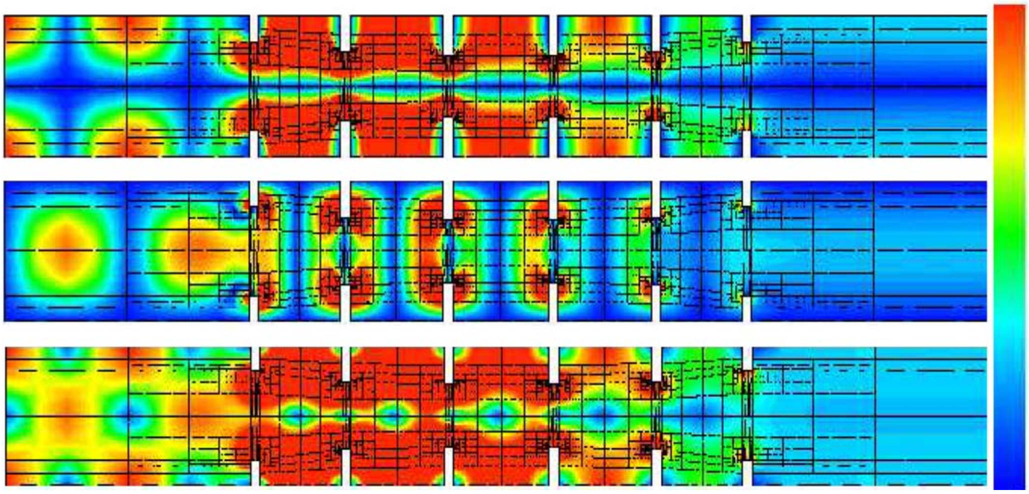

Fig. 31. $|H_x|$ (upper figure), $|H_y|$ (center figure), and $\sqrt{|H_x|^2 + |H_y|^2}$ (lower figure) at 8.72 GHz for the six irises waveguide problem. Different colors correspond to different values of the solution, from 0 (blue) to 1 (red).

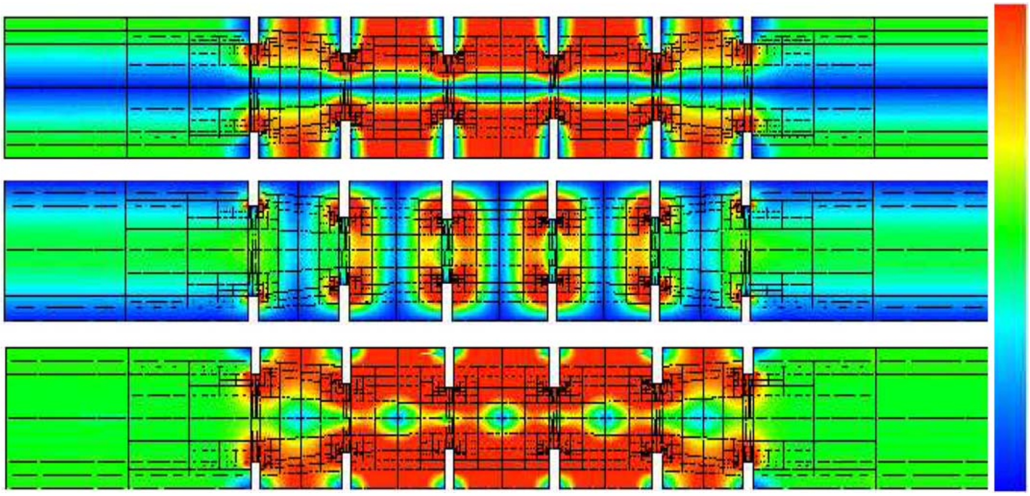

Fig. 32. $|H_x|$ (upper figure), $|H_y|$ (center figure), and $\sqrt{|H_x|^2 + |H_y|^2}$ (lower figure) at 8.82 GHz for the six irises waveguide problem. Different colors correspond to different values of the solution, from 0 (blue) to 1 (red).

5.2.3. Numerical results

The problem may be solved by using semi-analytical techniques (for example, mode matching techniques [27]). Nevertheless, it would be desirable to solve it using purely numerical techniques, since a numerical method allows for simulation of more complex geometries and/or artifacts possibly needed for the construction of an actual waveguide.

While attempting to solve this problem using the fully automatic *hp*-adaptive strategy coupled with the two grid solver, we encountered the following limitations:

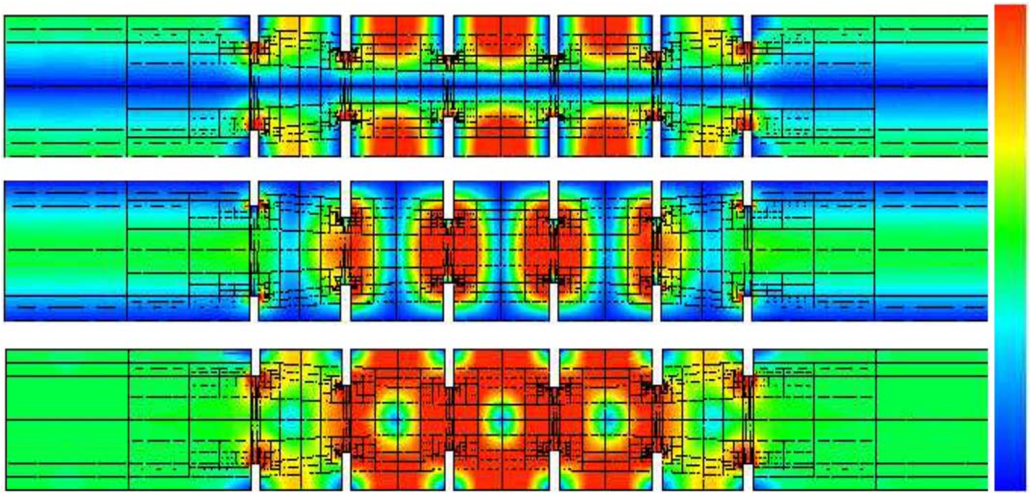

Fig. 33. $|H_x|$ (upper figure), $|H_y|$ (center figure), and $\sqrt{|H_x|^2 + |H_y|^2}$ (lower figure) at 9.58 GHz for the six irises waveguide problem. Different colors correspond to different values of the solution, from 0 (blue) to 1 (red).

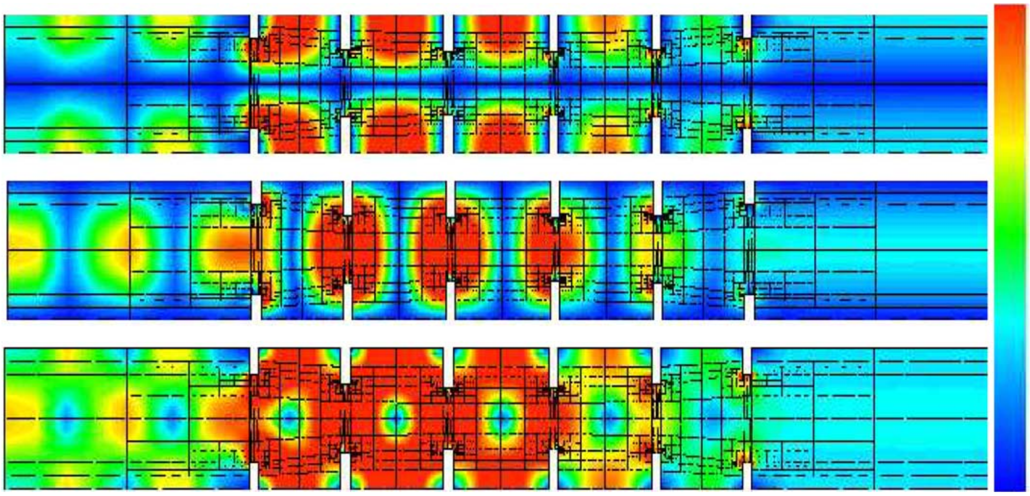

Fig. 34. $|H_x|$ (upper figure), $|H_y|$ (center figure), and $\sqrt{|H_x|^2 + |H_y|^2}$ (lower figure) at 9.71 GHz for the six irises waveguide problem. Different colors correspond to different values of the solution, from 0 (blue) to 1 (red).

(1) *We cannot guarantee convergence of the two grid solver if the coarse grid is not fine enough*, as predicted by the theory. In this case, we need a minimum of seven elements per wavelength λ in the x-direction, and thirteen elements per wavelength λ in the y-direction. Furthermore, as indicated in Table 1, convergence (or not) of the two grid solver is (almost) insensitive to p-enrichment.

(2) *We cannot guarantee the optimality of the fully automatic hp-adaptive strategy if the dispersion error is large.* Since solution of the problem on the fine grid is used to guide optimal *hp*-refinements, we need to control the dispersion error on the fine grid. Thus, h needs to be sufficiently small or p sufficiently large. In Fig. 29, we compare the convergence history obtained by using the fully automatic

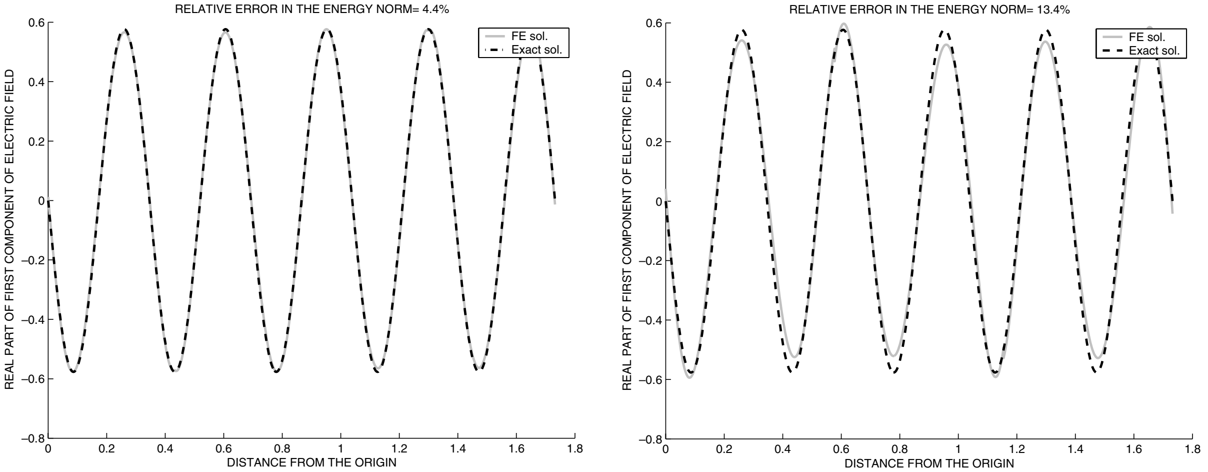

Fig. 35. 3D EM model problem. 1D cross section over the main diagonal of the unit cube (from (0,0,0) to (1,1,1)). Comparison between the exact and the FE solution component $Re(E_1)$, for different *hp*-meshes delivering 4.4% and 13.4% error (in the relative energy norm) respectively.

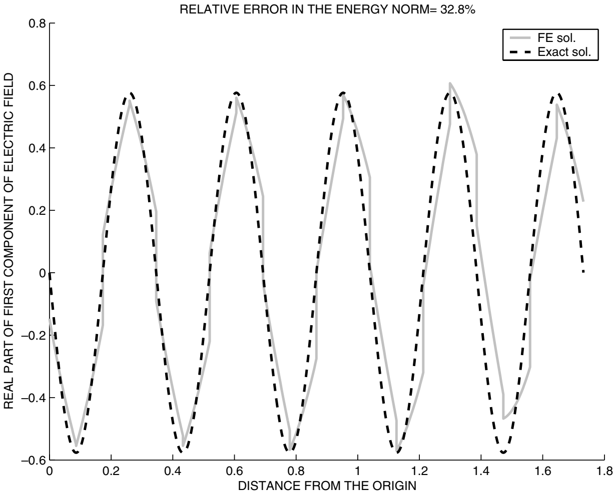

Fig. 36. 3D EM model problem. 1D cross section over the main diagonal of the unit cube (from (0,0,0) to (1,1,1)). Comparison between the exact and the FE solution component $Re(E_1)$, for an *hp*-mesh delivering 32.8% error (in the relative energy norm).

hp-adaptive strategy starting with different initial grids. For third order elements, the dispersion error is under control (see estimates of [1,20,21]), and the fully automatic *hp*-adaptive strategy converges exponentially. We also observe that, in the asymptotic regime, all curves present similar rates of convergence.

We solved the six irises waveguide problem delivering a 0.2% error (in the relative energy norm). Fig. 30 displays the magnitude of the S_{11} scattering parameter (on the decibel scale) with respect to the frequency. This quantity is usually referred to as the return loss of the waveguide structure. For frequency interval 8.8–

Table 2
3D electromagnetics model problem

No. of λ vs p	$p = 1$	$p = 2$	$p = 3$	$p = 4$	$p = 5$
$\lambda = 1$					
Error	5.0%	4.2%	1.2%	1.8%	0.3%
Elem/λ	20	3	2	1	1
d.o.f.	40K	946	1033	308	548
$\lambda = 2$					
Error		4.2%	2.9%	1.9%	0.3%
Elem/λ		3	1.5	1	1
d.o.f.	(>300K)	6427	2764	2226	4109
$\lambda = 3$					
Error		3.5%	4.1%	1.8%	2.1%
Elem/λ		3.33	1.33	1	0.66
d.o.f.	(>1200K)	31K	7115	6148	4109
$\lambda = 4$					
Error			5.0%	1.9%	1.2%
Elem/λ			1.25	1	0.75
d.o.f.	(>2300K)	(>82K)	12K	14K	12K
$\lambda = 5$					
Error			3.6%	4.4%	3.4%
Elem/λ			1.4	0.8	0.6
d.o.f.		(>135K)	31K	27K	12K
$\lambda = 6$					
Error			4.2%	3.8%	2.1%
Elem/λ			1.33	0.83	0.66
d.o.f.		(>240K)	46K	27K	27K
$\lambda = 7$					
Error				3.4%	4.3%
Elem/λ				0.86	0.57
d.o.f.		(>410K)	(>98K)	45K	27K
$\lambda = 8$					
Error					2.8%
Elem/λ					0.625
d.o.f.	(>20M)	(>650K)	(>167K)	(>71K)	51K
$\lambda = 50$					
Error					
Elem/λ					
d.o.f.	(>5000M)	(>122M)	(>25M)	(>14M)	(>9.5M)

For frequencies from 1 to 50 wavelengths λ, and uniform *hp*-grids ($1 \leqslant p \leqslant 5$), we display relative error in the energy norm (in percentage), number of elements per wavelength λ, and actual (or estimated) number of d.o.f. required to obtain an error below 5%.

9.6 GHz, the return loss is below −20 dB, which indicates that almost all energy passes through the structure, and thus, the waveguide acts as a filter.

Finally, Figs. 31–34 display solution at different frequencies. For frequencies 8.72 GHz, and 9.71 GHz, the return loss of the waveguide structure is large, and for frequencies 8.82 GHz, and 9.58 GHz the return loss is below −20 dB.

5.3. Analysis of a 3D EM model problem

In this section, we study numerically a 3D EM model problem introduced in Section 4.1.3. Given a unit cube geometry, the objective is to determine number of elements N and corresponding order of approximation p, needed to solve Maxwell's equations numerically, for an arbitrary plane wave solution at different frequencies (thus, wavelengths).

A second motivation for this numerical experiment comes from studying the fully automatic *hp*-adaptive strategy, which may produce misleading results if dispersion error on the initial fine grid is too large. In this section, we present combinations of uniform *hp*-grids, that lead to solution of our model problem (at different frequencies) with a relative energy norm error below 5%. These *hp*-meshes may be utilized as a guide to construct the initial fine grid for the *hp*-adaptive strategy.

For these purposes, we select an incoming plane wave with

$$\mathbf{k} = k(\sin(\alpha)\cos(\beta)\mathbf{u_x} + \sin(\alpha)\sin(\beta)\mathbf{u_y} + \cos(\beta)\mathbf{u_z}), \tag{5.110}$$

where k is the wave number, $\alpha = 35\pi/180$, and $\beta = 25\pi/180$. We consider a 1D cross section given by the main diagonal of the unit cube, starting at the origin and ending at point $(1,1,1)$. Figs. 35 and 36 show a comparison between exact and FE solution for the real part of the first component of the electric field, using different *hp*-meshes. For an *hp*-grid delivering 4.4% relative error in the energy norm, differences in both phase and amplitude between exact and FE solutions cannot be appreciated. As the error increases, these differences become larger.

Since solution of the 3D EM problem is smooth, large elements with large polynomial order of approximation p are preferred over small elements with small p. In addition, dispersion error decreases faster by increasing p rather than by decreasing element size h (see [1,20], and [21]). Table 2 illustrates these assertions. Using $p = 5$, a grid with 51000 d.o.f. delivers smaller error than a grid with 20 million unknowns and lowest order elements for the model problem with 8 wavelengths on the main diagonal.

Table 2 has been generated by using a direct (frontal) solver. Notice that the two grid solver requires an elevated number of elements per wavelength on the coarse grid to guarantee convergence, as mentioned in Section 5.2. As a consequence, the two grid solver could not be utilized to produce the table.

6. Conclusions and future work

In this paper, we have studied a two grid solver for solving linear systems resulting from *hp* FE discretizations of Maxwell's equations. The meshes come in pairs, consisting of a coarse mesh and the corresponding fine mesh obtained via the global *hp* refinement of the coarse mesh. The coarse meshes are generated by a special *hp*-adaptive algorithm, based on minimizing the projection based interpolation error of the fine mesh solution with respect to the next optimally refined coarse mesh. The solver combines block Jacobi smoothing with an optimal relaxation, with the coarse grid solve.

Instead of using the two grid iteration for producing a preconditioner for conjugate gradient (CG) only, we chose to accelerate each smoothing operation individually with an approximation of the steepest descent (SD) method, which we interpret as determining the optimal relaxation parameter.

Within the described framework, we have studied several critical questions including the convergence theory, implementation issues, the need of controlling gradients, error estimation for the two grid solver and, first of all, the possibility of guiding the *hp* strategy for EM problems with only partially converged solution. As a result of it, we verified that a partially converged solution, with a rather large (relative) error tolerance of 0.1, is sufficient to guide the *hp* strategy. The corresponding number of two grid iterations stays then very minimal at a level below 10 iterations per mesh.

Then, we have applied our numerical technique (the fully automatic *hp*-adaptive strategy coupled with the two grid solver) to a number of practical EM problems. While most applications were solved with extreme accuracy, we also faced a number of limitations:

- The two grid solver may not converge for indefinite problems if the coarse grid is too coarse. Furthermore (as shown in Lemma 1), this condition over the element size *does not* depend upon the polynomial order of approximation p. A multigrid solver for which the constant in Lemma 1 decreases as p increases is badly needed for wave propagation problems, when *hp*-finite elements are used.
- An adaptive strategy based on minimization of the energy norm may be inadequate for a number of EM applications as, for example, the axisymmetric battery antenna problem. Thus, an *hp* goal-oriented adaptive algorithm is needed.

Acknowledgements

The work has been partially supported by Air Force under Contract F49620-01-1-0043 and NSF under Grant DMS-0410030. The computations reported in this work were done through the National Science Foundation's National Partnership for Advanced Computational Infrastructure.

References

[1] M. Ainsworth, Discrete dispersion relation for *hp*-version finite element approximation at high wave number, SIAM J. Numer. Anal. 42 (2) (2004) 553–575.

[2] D.N. Arnold, R.S. Falk, R. Winther, Multigrid in *H*(div) and *H*(curl), Numer. Math. 85 (2000) 197–217.

[3] D. Boffi, M. Costabel, M. Dauge, L. Demkowicz, Discrete compactness for the *hp*-version of rectangular edge finite elements, ICES Report 04-29, 2004.

[4] D. Boffi, L. Demkowicz, M. Costabel, Discrete compactness for *p* and *hp* 2D edge finite elements, Math. Models Methods Appl. Sci. 13 (2003) 1673–1687.

[5] J.H. Bramble, Multigrid MethodsPitman Research Notes in Mathematics Series 294, vol. viii, Longman Scientific & Technical, Harlow, 1993, 161 p.

[6] X. Cai, O.B. Widlund, Domain decomposition algorithms for indefinite elliptic problems, SIAM J. Sci. Stat. Comput. 13 (1992) 243–258.

[7] M. Cessenat, Mathematical Methods in Electromagnetism. Linear Theory and ApplicationsSeries on Advances in Mathematics for Applied Sciences, vol. 41, World Scientific Publishers, Singapore, 1996.

[8] L. Demkowicz, Edge finite elements of variable order for Maxwell's equations, in: Van Rienen Ursula et al. (Eds.), Scientific Computing in Electrical Engineering. Proceedings of the 3rd International Workshop, Warnemünde, Germany, August 20–23, 2000, Lect. Notes Comput. Sci. Engrg., vol. 18, Springer, Berlin, 2001, pp. 15–34.

[9] L. Demkowicz, *hp*-Adaptive finite elements for time-harmonic Maxwell equations, in: Ainsworth Mark et al. (Eds.), Topics in Computational Wave Propagation. Direct and Inverse Problems, Lect. Notes Comput. Sci. Engrg., vol. 31, Springer, Berlin, 2003, pp. 163–199.

[10] L. Demkowicz, I. Babuska, *p*-Interpolation error estimates for edge finite elements of variable order in two dimensions, SIAM J. Numer. Anal. 41 (2003) 1195–1208.

[11] L. Demkowicz, A. Buffa, H^1, $H(\mathbf{curl})$, and $H(\mathrm{div})$ conforming projection-based interpolation in three dimensions: quasi optimal p-interpolation estimates, Comput. Methods Appl. Mech. Engrg. 194 (2005) 267–296.

[12] L. Demkowicz, P. Monk, L. Vardapetyan, W. Rachowicz, The Rham diagram for *hp* finite element spaces, Tech. Rep. 99-07, TICAM Report, 1999.

[13] L. Demkowicz, W. Rachowicz, P. Devloo, A fully automatic *hp*-adaptivity, J. Sci. Comput. 17 (2002) 117–142.
[14] J. Gopalakrishnan, L.F. Demkowicz, Quasioptimality of some spectral mixed methods, J. Comput. Appl. Math. 167 (2004) 163–182.
[15] J. Gopalakrishnan, J.E. Pasciak, Overlapping Schwarz preconditioners for indefinite time harmonic Maxwell equations, Math. Comput. 72 (2003) 1–15.
[16] J. Gopalakrishnan, J.E. Pasciak, L. Demkowicz, Analysis of a multigrid algorithm for time harmonic Maxwell equations, SIAM J. Numer. Anal. 42 (2004) 90–108 (electronic).
[17] R.F. Harrington, Time-Harmonic Electromagnetic Fields, McGraw-Hill, New York, 1961.
[18] A. HarveyMicrowave Engineering, vol. XLII, Academic Press, London, 1963, 1313 p.
[19] R. Hiptmair, Multigrid method for Maxwell's equations, SIAM J. Numer. Anal. 36 (1998) 204–225.
[20] F. Ihlenburg, I. Babuska, Finite element solution of the Helmholtz equation with high wave number. I: the *h*-version of the FEM, Comput. Math. Appl. 30 (1995) 9–37.
[21] F. Ihlenburg, I. Babuska, Finite element solution of the Helmholtz equation with high wave number. II: The *h–p* version of the FEM, SIAM J. Numer. Anal. 34 (1997) 315–358.
[22] J. Meixner, The behavior of electromagnetic fields at edges, IEEE Trans. Antennas Propag. 20 (1972) 442–446.
[23] P. Monk, A simple proof of convergence for an edge element discretization of Maxwell's equations, in: Computational electromagneticsLect. Notes Comput. Sci. Engrg., vol. 28, Springer, Berlin, 2003, pp. 127–141.
[24] J. Nedelec, Mixed finite elements in $\mathbb{R}^3$, Numer. Math. 35 (1980) 315–341.
[25] D. Pardo, L. Demkowicz, Integration of *hp*-adaptivity with a two grid solver for elliptic problems, Tech. Rep. 02-33, TICAM Report, 2002.
[26] B.F. Smith, P.E. Bjrstad, W.D. Gropp, Domain decomposition. Parallel multilevel methods for elliptic partial differential equations, Cambridge University Press, Cambridge, 1996.
[27] Guided wave technology, www.guidedwavetech.com.
[28] J. Xu, Iterative methods by space decomposition and subspace correction, SIAM Rev. 34 (1992) 581–613.